ACS APPLIED NANO MATERIALS

www.acsanm.org Article

Nickel-Embedded Carbon Nanostructures as Noble Metal-Free Catalysts for the Hydrogen Evolution Reaction

Sarvesh Kumar, Rajeev Kumar, Naveen Goyal, Ankit Yadav, Swetha BM, and Balaram Sahoo*

Cite This: https://doi.org/10.1021/acsanm.4c02278 Read Online

ACCESS | Metrics & More | Article Recommendations | Supporting Information

ABSTRACT: We demonstrate the electrocatalytic activity of "nitrogen (N)-doped porous carbon matrix embedded with nickel nanoparticles" for efficient hydrogen evolution reaction (HER) in alkaline medium. Three samples were synthesized via pyrolysis of a fixed amount (500 mg) of $Ni(acac)_2$, along with three different amounts of nitrogen precursor melamine (100, 250, and 500 mg) separately. The varying nitrogen concentrations of the surrounding carbon layers on the Ni nanoparticles enhance the surface area and porosity, exposing extensive active sites for catalytic reactions. The transition metal-based catalysts are crucial for long-term sustainability due to their combined edge (effectiveness and inexpensiveness) over traditional catalysts. Thus, by employing the protective carbon layer on the transition metal nanoparticles, we fabricated a catalyst that exhibits outstanding performance, with a low overpotential of 45.6 mV at 10 mA cm^{-2} in 1 M KOH and maintains it for 24 h (durability), highlighting its exceptional catalytic efficacy and stability. The pores in carbon nanostructures facilitate the ionic moieties to move to active sites inside the pores. As the pore size variation influences the movement of charge or diffusion, this is reflected in the magnitude of impedance ($|Z|_{imp}$). Consequently, the enhanced number of active sites along with the larger pore sizes resulting from optimum amounts of nitrogen doping enables the sample with minimal $|Z|_{imp}$ and an enhanced HER performance. The present study demonstrates the way to design a sustainable, extremely effective, and inexpensive HER electrocatalyst.

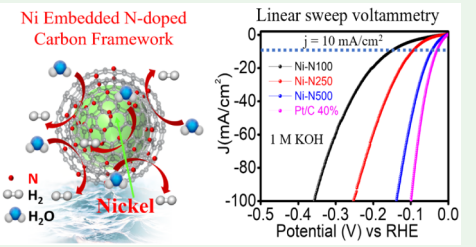

KEYWORDS: *N-doped carbon, Ni nanoparticles, electrocatalyst, hydrogen evolution reaction, basic medium, EIS*

1. INTRODUCTION

A practical and effective method for generating green energy, such as producing hydrogen from the abundant resource of water, is essential to meet the world's increasing energy demands.[1] However, directly producing hydrogen by splitting water naturally is almost impossible, so a catalyst is required. Furthermore, generating hydrogen from water through direct electrolysis is extremely difficult.[2] Hence, emphasis has been made on effective transition metal-based traditional electrocatalysts such as Pt, Au, and Ag,[3,4] which are too expensive. On the other hand, the hydrogen evolution reaction (HER) can be catalyzed in two different ways: (1) from hydrogen ions available in an acidic medium through the dissociation of the acid[5] and (2) through the dissociation of water in a basic medium.[6] While extracting hydrogen from acid is relatively straightforward, it is not cost-effective. Extracting hydrogen from water in a basic medium poses challenges, necessitating a suitable, stable, inexpensive, and efficient catalyst. Although traditional catalysts are viable options, their significant cost is a disadvantage and a limitation. Therefore, we aim to showcase 3d-transition metal (TM) elements (such as Fe, Co, and Ni) as catalysts. The primary concern with these metals is their susceptibility to corrosion in both water and acidic mediums.[7] Yadav et al. have shown that coating metallic particles with a reduced graphene oxide sheet can effectively shield the 3d-transition metal particles in a highly corrosive environment.[8−11] Moreover, Kumar et al. have conducted thorough research on synthesizing and controlling the graphitic properties of carbon on the embedded 3d-transition metal nanoparticles.[12−14] Earlier, significant efforts were devoted to developing a low-cost 3d-transition metal-based catalyst;[15−17] however, their stability and multifunctionality have not been thoroughly explored. Numerous noteworthy attempts are underway to design alternative catalysts suitable for the hydrogen evolution reaction (HER).[18,19] These catalysts have the potential to replace those reliant on precious metals.

Hydrogen generation is constrained by the high overpotential and low chemical stability of existing catalysts for water electrolysis.[20,21] Researchers have previously explored earth-abundant and stable transition metals as catalysts, such as (Fe, Co, Ni)-oxides,[22] -nitrides,[23] and -carbides,[24] but their efficiency is constrained by poor intrinsic conductivity. Moreover, to optimize the catalytic performance of 3d-transition metal particles, durable, conductive, and anticorrosive supports such as carbon cages, nanotubes, or nanorods

Received: April 29, 2024
Revised: June 17, 2024
Accepted: June 18, 2024

need to be developed.[25] Fei et al.[1] recently reported that metal nanoparticles embedded in a carbon framework create stable and effective electrocatalysts for the hydrogen evolution reaction (HER). The graphenic coating on metal nanoparticles prevents oxidation and synergistically enhances electrocatalytic activity, with its effectiveness influenced by the thickness of the carbon layer.[25−27] To shield these 3d-transition metal nanoparticles from corrosion and enhance catalytic performance through N-doping, we endeavored to embed the nanoparticles in a N-doped porous carbon matrix.

Herein, we present a cost-effective, scalable, and single-step synthesis method for producing porous nanostructured nitrogen-enriched graphitized-carbon-coated nickel nanoparticles under an inert atmosphere, as illustrated in Scheme 1.

Scheme 1. Schematic Presentation of the Synthesis of Ni−NY (Y= 100, 250, and 500) Samples

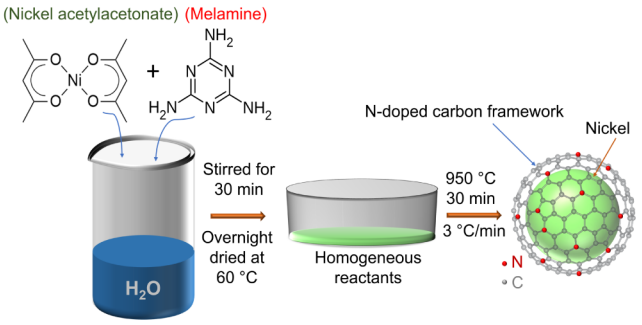

The variation in N-doping induces a porous architecture, providing a large specific surface area, porosity, and exposed active centers, facilitating the adsorption of hydrogen atoms. Optimizing the loading of catalyst supports is crucial for overcoming constraints. Additionally, the confined porous geometry prevents the agglomeration of graphitic carbon-coated Ni nanoparticles, thereby enhancing the performance of diverse electrocatalytic active centers. The active sites generated from nitrogen doping accelerate the kinetics more rapidly. Moreover, we demonstrate here that these HER electrocatalysts exhibit high efficiency and stability, displaying excellent electrocatalytic performance and long-term stability in an alkaline medium.

2. RESULTS AND DISCUSSION

We synthesized Ni nanoparticles coated with graphitic carbon shells doped with varying amounts of nitrogen (Ni−NY, where Y = 100, 250, and 500) as catalysts for the HER. Scheme 1 illustrates the synthesis procedure, while the experimental details can be found in Section S1 of the electronic Supporting Information file accompanying this paper. The study of the structure and active centers for the HER activity in Ni−NY catalysts is crucial for understanding the efficient extraction of green hydrogen from water. Hence, a detailed analysis of the structural aspects of samples is given below.

2.1. Structural Investigation. *2.1.1. X-ray Diffraction (XRD).* Figure 1a presents the X-ray diffraction (XRD) patterns of Ni−NY (Y = 100, 250, and 500) powder samples within the 2θ range of 10° and 60°, revealing three peaks. Specifically, the peak at 26.5° corresponds to the (002) plane of graphitic carbon, while the peaks at 44.5° and 51.8° correspond to the (111) and (200) planes of the face-centered cubic (fcc) phase in metallic nickel (Ni) nanoparticles, respectively. This

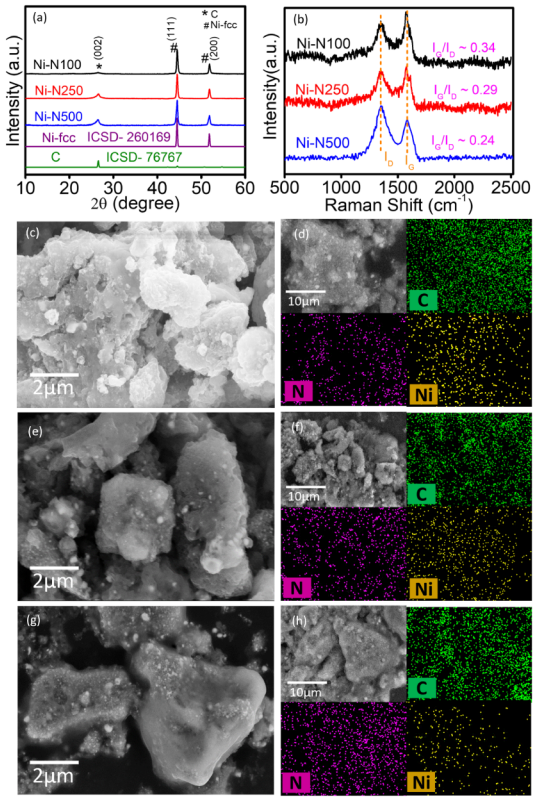

Figure 1. (a) XRD patterns recorded on Ni−NY samples and well matched with ICSD data of C (File # 76767) and Ni (File # 260169). (b) Raman spectra of Ni−NY samples. The SEM images were recorded on (c) Ni−N100, (e) (Ni−N250), and (g) Ni−N500 samples. The SEM (10 μm scale) micrograph with EDX elemental mapping for C, N, and Ni, respectively, for (d) Ni−N100, (f) (Ni−N250), and (h) Ni−N500 samples.

indicates the presence of two distinct phases. The peaks detected in the XRD pattern match well with the inorganic crystal structure database (ICSD) entries for Ni-fcc (ICSD-260169) and C (ICSD-76767). Interestingly, a visual inspection of the XRD patterns reveals that the line widths of the Ni (111) and (200) Bragg peaks increase with the amount of melamine. This implies the presence of the smallest metallic crystallites in the Ni−N500 sample. The broadening of the (002) Bragg peak suggests the presence of both amorphous and graphitic carbons in the material. This observation is confirmed by the fitting of two subpeaks, indicating the presence of amorphous carbon (a-C) and graphitic carbon (g-C) (Figure S1). As the amount of amorphous carbon in the samples decreases, the a-C to g-C ratio (a-C/g-C) also decreases. The a-C concentrations in the Ni−N100, Ni−N250, and Ni−N500 samples are approximately 38.5%, 24.6%, and 22.5%, respectively, as shown in Table S1. This suggests that increasing the melamine content leads to enhanced graphitization. A detailed discussion of these aspects is provided in Supporting Information, Section S2 1.1. Consequently, the ratio of a-C to g-C decreases as the amount of amorphous carbon gradually diminishes in the sample. The broadening of carbon peaks can be attributed to the presence of doped nitrogen atoms and intrinsic defects.[28]

To gain a comprehensive understanding of the catalytic performance resulting from N-doping and the presence of metal nanoparticles in the samples, we synthesized similar

https://doi.org/10.1021/acsanm.4c02278
ACS Appl. Nano Mater. XXXX, XXX, XXX−XXX

samples without N-doping and without the presence of metal. Specifically, we prepared reduced graphene oxide using an improved Hummers' method[10] and characterized it. The XRD pattern of the nickel-embedded carbon matrix without N-doping (sample code: Ni−C) exhibits peaks similar to those observed in Ni−NY samples, as illustrated in Figure S1g. In contrast, both the reduced graphene oxide (rGO) and N-doped rGO show a peak at approximately 2θ of 26.6°, corresponding solely to the C (002) peak.

2.1.2. Raman Spectroscopy. Raman spectra of the Ni−NY samples are listed in Figure 1b. Notably, two prominent peaks at ∼1351 and ∼1575 cm^{-1} indicate the presence of defective carbon (D-band) and graphitic carbon (G-band), respectively. Deconvoluting the Raman spectra offers vital insights into the defects. Hence, we conducted fitting into subpeaks (the details of the subpeaks and their positions are mentioned Section S2 1.2). It is important to note that the increase in the D-band intensity can be correlated with the rise in the amount of foreign (nitrogen) atoms inserted into the carbon layer.[29] The ratio of the intensity of the graphitic (G) peak to the defective (D) peak (I_G/I_D) provides a quantitative measure of the total surface defects in the carbon structure.[30,31] This ratio is found to be 0.34, 0.29, and 0.24 for the Ni−N100, Ni−N250, and Ni−N500 samples, respectively (Table S2). Hence, the graphitic crystallites of the Ni−N500 sample are less defect-enriched (amorphous) than the other samples, as made evident by the previously reported XRD results. The intensity ratio I_{D1}/I_G serves as an indicator of planar defects in the samples. As shown in Table S2 and the corresponding plot in Figure S7a, the increase in I_{D1}/I_G with increasing melamine content demonstrates that a higher amount of nitrogen precursor during synthesis leads to a rise in the number of planar defects. The I_{D2}/I_G intensity ratio provides information regarding carbon atoms at the edges of graphitic crystallites, and the I_{D3}/I_G ratio represents the amount of amorphous carbon present in the samples. This aspect will be discussed more in the XPS results. Hence, Raman analysis offers valuable insights into the quantities and types of local defects present in the samples. The presence of these defects primarily promotes the formation of electrochemically active centers,[32] leading to a substantial enhancement in the HER activity.

2.1.3. Scanning and Transmission Electron Microscopy (SEM and TEM). The SEM micrographs of the synthesized Ni−N100, Ni−N250, and Ni−N500 samples are displayed in Figure 1c,e, and g, respectively. The micrographs clearly show that all the samples contain several carbon aggregates, specifically depicting two intensity levels: white and gray. The white regions indicate the presence of Ni nanoparticles on the nanoscale. This is because Ni atoms emit more secondary electrons than carbon atoms, resulting in carbon appearing gray in contrast. The appearance of the white and gray region in micrographs is described in depth in Section S2 1.3. SEM micrographs depict gray areas, indicating the presence of carbonaceous material (carbon flakes), with irregular shapes observed across all synthesized samples. As previously discussed, this is understandable and given that higher carbon content in the Ni−N500 sample leads to enhanced dispersion of the metallic nanoparticles within the matrix. The SEM images of the Ni−C, N-doped rGO, and rGO samples are shown in Figure S2a−c, respectively. In comparison, the morphology of the Ni−C sample appears to be similar to that of the Ni−NY sample. The SEM images for energy dispersive X-ray (EDX) elemental distribution are shown in Figure 1d,f, and h, for Ni-N100, Ni-N250, and Ni-N500, respectively.

In the EDX mapping, we observed a uniform distribution of all elements, including C, N, and Ni, throughout the samples. However, as expected, a denser distribution of nitrogen (N) was observed with increasing amounts of the melamine precursor, as shown in Figure 1f. Conversely, it was observed that the quantity of dispersed Ni nanoparticles within the scanned area decreased as the concentration of melamine increased in the samples, despite the use of an identical quantity of Ni precursor (750 mg of $Ni(acac)_2$) during synthesis. This decrease is attributed to the additional contribution of carbon atoms from the melamine precursor. A detailed explanation of this observation is provided in Supporting Information Section S2 1.3.1, Table S3, and Figure S2d. TEM was employed for further structural characterization. Figure 2a−c depicts bright-field TEM micrographs of the Ni−N100, Ni−N250, and Ni−N500 samples, respectively. It was observed that all of the Ni nanoparticles were encased in a

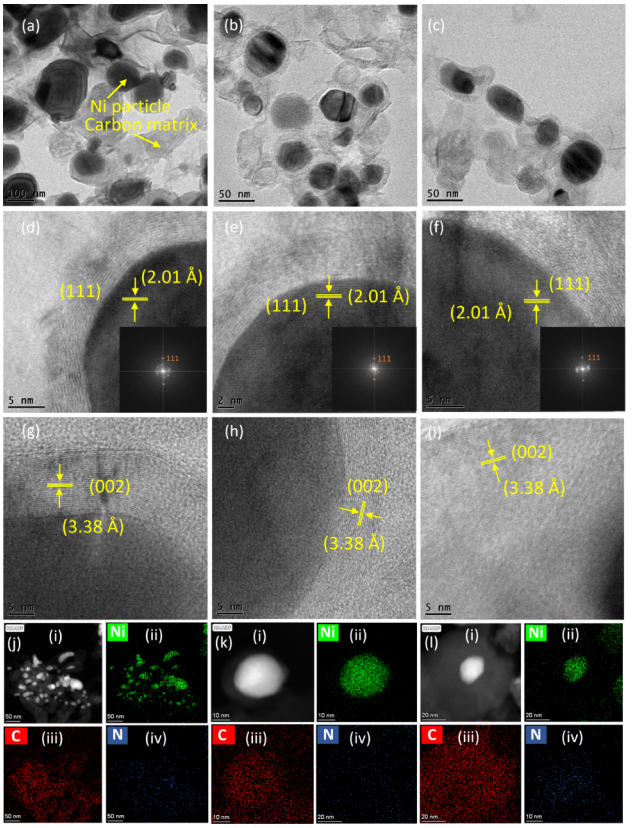

Figure 2. (a), (b), and (c) show the low-magnification bright-field TEM micrographs of Ni−N100, Ni−N250, and Ni−N500 samples, respectively. HRTEM image of Ni nanoparticle present in the corresponding sample shown in (d), (e), and (f). Inset shows related FT of HRTEM image. HRTEM image of carbon matrix around Ni nanoparticle in corresponding Ni-N100, Ni-N250, and Ni-N500 samples are shown in (g), (h), and (i), respectively. (j)(i) High-angle annular dark-field scanning transmission electron microscopy (HAADF-STEM) of Ni−N100 sample, while (ii), (iii), and (iv) show the elemental mapping for Ni, C, and N, respectively. (k)(i) HAADF- STEM image of Ni−N250 sample, while (ii), (iii), and (iv) show the elemental mapping for Ni, C, and N, respectively. (l)(i) HAADF- STEM image of Ni−N500 sample, while (ii), (iii), and (iv) show the elemental mapping for Ni, C, and N, respectively.

https://doi.org/10.1021/acsanm.4c02278
ACS Appl. Nano Mater. XXXX, XXX, XXX−XXX

graphitic carbon shell. Figure 2d–f displays HRTEM images of Ni nanoparticles encased in a graphitic carbon shell for each sample. The *d*-spacing value of approximately 2.01 Å, corresponding to the (111) plane of the Ni fcc lattice, confirms the core–shell configuration of Ni-graphitic-C. For a detailed view of atomic arrangement, the zoomed-in Ni (111) fcc lattice is shown in Figure S3. The fast Fourier transform of the Ni nanoparticles' lattice fringes is inset in each HRTEM image (Figure 2d–f). The bright spot confirms the presence of the (111) plane of the Ni-fcc lattice, also evident in the XRD pattern of all synthesized samples. The HRTEM images of the graphitic carbon shells for Ni–N100, Ni–N250, and Ni–N500 samples, revealing resolved lattice fringes (with a *d*-spacing of approximately 3.38 Å consistent with the (002) plane of carbon), are presented in Figure 2g–i, respectively. Figure 2j(i) illustrates the high-angle annular dark-field scanning transmission electron microscopy (HAADF-STEM) image of the Ni–N100 sample, accompanied by elemental mapping depicting the distribution of Ni, C, and N in (ii), (iii), and (iv) respectively. In Figure 2k(i), the HAADF-STEM image of the Ni–N250 sample is presented, along with the corresponding elemental distribution of Ni, C, and N shown in (ii), (iii), and (iv), respectively. The HAADF-STEM image of the Ni–N500 sample is shown in Figure 2l(i), followed by the elemental distributions of Ni, C, and N in parts ii, iii, and (iv), respectively.

2.1.4. X-ray Photoelectron Spectroscopy (XPS). X-ray photoelectron spectroscopy (XPS) was employed to analyze the elemental composition of the Ni–NY (Y = 100, 250, and 500) samples. The high-resolution XPS (HRXPS) spectra of C 1s, N 1s, and Ni 2p are presented in Figure S6. The inclusion of nitrogen atoms into the carbon matrix alters the electronic structure, enhancing their electrocatalytic activity.[12,33] The highly delocalized electrons within this pristine graphitic network exhibit lower chemical activity, limiting their involvement in electrochemical reactions[14] (further details of this aspect are discussed, Section S2 1.5). The presence of nitrogen within the carbon structure increases the reactivity by inducing defects and altering electronic delocalization, prompting chemical reactions. Normally, in pristine graphitic carbon, π electrons from carbon 2p orbitals strongly overlap, forming highly delocalized planes both above and below the graphenic sheets of σ-bonded carbon layers.[34,35] However, the introduction of nitrogen disrupts this electron continuity due to the electronegativity difference between carbon (2.55) and nitrogen (3.05), rendering the sample more reactive compared to pristine carbon sheets.[36] Differences in the nitrogen concentration among Ni–NY samples affect electronic delocalization and the electronic environment, influencing their participation in electrochemical reactions. The XPS peak positions and their full width at half-maximum (fwhm) obtained from the least-squares fittings for the C 1s, N 1s, and Ni 2p spectra are listed in Table S4. The total carbon content was determined to be 54.7%, 69.5%, and 81.8% for the Ni–N100, Ni–N250, and Ni–N500 samples, respectively.

In literature, the lesser electron-withdrawing nature of the carbon framework is noticed as a small fwhm, whereas strongly influenced electronic delocalization gives rise to a highly withdrawing nature as a large full width at half-maximum (fwhm).[37] Figure S5 illustrates nitrogen moieties including pyrrolic, pyridinic, and quaternary nitrogen, with electron density at neighboring carbon atoms. Due to the high electronegativity of N, the ortho-carbon of pyridinic N experiences a more positive charge cloud, while N has a negative charge cloud. The positive charge density at the ortho-carbon is lower for pyrrolic N and decreases even further for quaternary N.[38,39] The pyridinic nitrogen has a lower electron-withdrawing nature than the graphitic N because the lone pair remains neutral.[40] Among all types of nitrogen, pyridinic and pyrrolic nitrogen species easily coordinate with nickel and form Ni–N_xC complex, which decreases the adsorption energy of neighboring carbon atoms.[41] The overall nitrogen content (atomic percentage) was found to be 2.3, 4.5, and 7.2% for Ni–N100, Ni–N250, and Ni–N500 samples (Table S5), respectively, and the relative amounts of different nitrogen moieties are shown in Figure 3a.

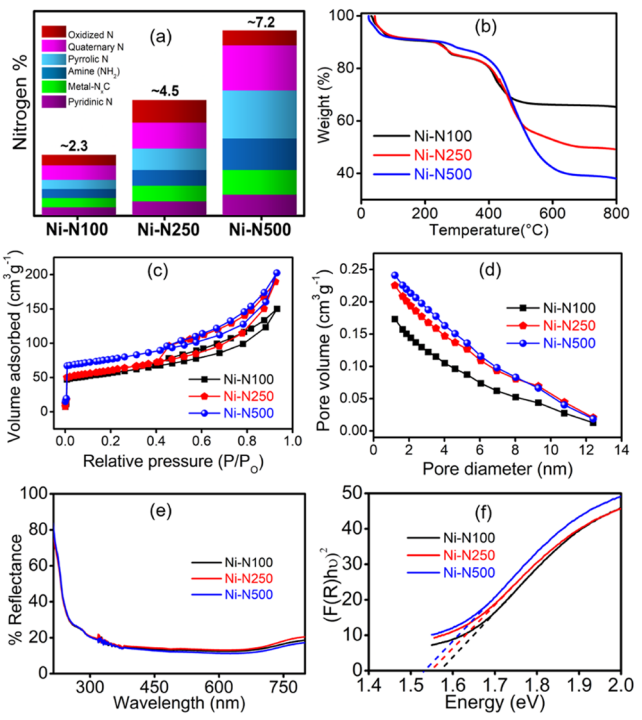

Figure 3. (a) Percentage of nitrogen content in material as derived from XPS results, (b) TGA profile, (c) N_2 adsorption/desorption BET curve, (d) distribution of pores, (e) UV vis-DRS reflectance spectra, and (f) band gap estimation on Ni–NY (Y= 100, 250 and 500) samples, respectively.

The XPS scan of Ni 2p core–shells revealed the presence of nickel metal and various nickel species in the spectra. The assigned peaks indicate the existence of nickel metal, surface + nonlocal, and satellite peaks at specific energy levels (the details of this aspect are provided in Supporting Information, Section S2 1.5).[42] The amounts of nickel were found to be 43, 26, and 11% for the Ni–N100, Ni–N250, and Ni–N500 samples, respectively. It is notable that the fwhm (from XPS) of the main carbon peak for Ni–N500 (1.46 eV) is significantly broader compared to Ni–N100 and Ni–N250 (1.32 and 1.40 eV, respectively).[37] This is also evidenced by the Raman study, which shows the lowest I_G/I_D ratio for Ni–N500 among the Ni–N250 and Ni–N100 samples. The significant broadening observed in the main carbon peak strongly indicates a predominant association of nitrogen within the graphitic carbon plane.[37] To validate this phenomenon, we correlated the in-plane sp^2-induced defects (D1) from the Raman study with the fwhm of the main carbon peak in XPS.

https://doi.org/10.1021/acsanm.4c02278
ACS Appl. Nano Mater. XXXX, XXX, XXX–XXX

Ni−N500 showed the greatest interruption in electronic delocalization (large C 1s fwhm) and the highest in-plane defects (large I_{D1}/I_G), as seen in Figure S7a, with a linear correlation to the highest C 1s fwhm shown in Figure S7b. The defects at the edges of graphitic crystallites (I_{D2}/I_G) and amorphous carbon defects (I_{D3}/I_G) decrease with increasing N-doping, as shown in Table S2. This significant reduction in I_{D3}/I_G and I_{D2}/I_G in the Ni−N500 sample suggests that the defects are closely associated with graphitic carbon, altering the electronic properties and enhancing the electrochemical activity.

2.1.5. Thermogravimetry Analysis (TGA). The temperature-dependent decomposition of Ni−NY samples was examined using weight loss vs temperature curves from TGA in air, as shown in Figure 3b. Typically, thermal decomposition at various temperatures is attributed to the cleavage of C−C and C−N bonds. The amorphous carbon begins to combust at lower temperatures compared to the more structured carbon matrix.[43] Weight loss below ∼270 °C is due to the removal of surface functionalities. The thermal decomposition analysis shows a higher concentration of amorphous carbon in the Ni−N100 sample, as indicated by its earlier burning onset. The slightly higher decomposition temperature in the Ni−N500 sample suggests greater graphitization. Increasing the N-precursor typically results in more defective graphitic carbon due to nitrogen dopants, as seen in our Ni−NY samples. Additionally, higher melamine precursor amounts lead to an increased level of amorphous carbon, contributing to the total carbon content. This aspect is clearly discussed in Section 2.2. The highly graphitic heterostructure forms stronger covalent bonds compared to amorphous carbon.[44] The N-doped heterostructures in the lattice could enhance the chemisorption phenomenon of various volatile products, requiring temperatures between 100 and 300 °C for their expulsion.[44,45] Furthermore, the residual masses measured at temperatures exceeding 515, 600, and 650 °C for Ni−N100, Ni−N250, and Ni−N500 are 66.4%, 50.6%, and 39.6%, respectively. These values indicate the presence of Ni-fcc nanoparticles in the samples. The decreased residual content of 39.6% for Ni−N500, along with a slightly higher burning temperature, suggests a significant presence of graphitic-defected carbon, which correlates with the quantity of the melamine precursor used.

2.1.6. BET Analysis. Nitrogen adsorption/desorption isotherm technique was employed to determine the Brunauer−Emmett−Teller (BET) surface area and pore size distribution using the Barrett−Joyner−Halenda (BJH) approach, as depicted in Figure 3c,d. The plot in Figure 3c reveals that initially, the heterostructure sites were vacant, but with a slight increase in relative pressure, there was a rapid rise in adsorption volume below 0.05 P/P_o. With further pressure application, subsequent adsorption takes place either on the flat surface or through capillary condensation.[46,47] The versatile morphology of the heterostructures facilitates improved gas molecule penetration (these aspects are discussed in detail, Section S2.1.4). The specific BET surface area, volume of the pore, and mean pore diameter values for the Ni−N500 sample are 246.9 $m^2\ g^{-1}$, 0.301 $cm^3\ g^{-1}$, and 5.365 nm, respectively, which are superior to those of Ni−N100 (197.8 $m^2\ g^{-1}$, 0.232 $cm^3\ g^{-1}$, and 4.785 nm) and Ni−N250 (218.7 $m^2\ g^{-1}$, 0.293 $cm^3\ g^{-1}$, and 4.896 nm) samples. This large BET-specific surface area for the Ni−N500 sample, compared to Ni−N250 and Ni−N100, offers improved porosity and high surface structural defects.[48] These structural modifications are helpful for their catalytic activity.

2.1.7. UV Vis−DRS Analysis. The UV vis−visible diffuse reflectance spectra of as-synthesized samples Ni−NY (Y = 100, 250, and 500) were recorded in the 200−800 nm range and are shown in Figure 3e. The Kubelka−Munk method[13,49] estimates the band gap of materials (Section S2 1.6). The Kubelka−Munk plot depicted in Figure 3f reveals direct band gap values of 1.59 1.56, and 1.53 eV for the Ni−N100, Ni−N250, and Ni−N500 samples, respectively. The defects induced in the graphitic carbon shell by N-doping generate their unique energy states within the band gap of graphitic carbon's energy band. The spread of energy levels leads to the defect gradient and extends inside the bandgap. Hence, the electrochemical reaction is influenced by the type and extent of disorder in the material.[13] This effect can clearly visualized by plotting the Urbach energy plot (Figure S8a) for our samples, which signifies the spread of energy levels associated with defects within the band gap. Typically, these defect levels extend like a tail into the bandgap region (Figure S8b−d).[50] As a result, by adjusting the nitrogen doping, the distribution of the bands is determined by the nature of the disorder present in the sample.[12] This observation is further corroborated by the elevated I_{D1}/I_G in the Raman study and the significant fwhm of the C 1s main peak in XPS, as depicted in Figure S7b. Hence, as the catalytic features of the materials are largely influenced by their electronic band structure, and changes in the electronic structure have a significant impact on catalytic activity.

2.2. The Mechanism of Graphitization in the Samples. The pyrolytic growth of nickel nanoparticles-embedded graphitic-carbon follows the vapor−liquid−solid (VLS) mechanism, as discussed in many previous reports.[13,14,51] The mechanism of the graphitization process proceeds as follows. When the precursors ($Ni(acac)_2$ and melamine ($C_3N_6H_6$)) are heated, they decompose into carbon, nitrogen, and nickel vapors.[52] Among all the vapors, being heavier (having higher momentum) and having a higher adhesive nature, the nickel vapor is assumed to deposit on the walls of the quartz tube easily. Once deposited, the nickel atoms segregate and form small nanoparticles. Being small nanoparticles, they are in the molten state, even at approximately 400 °C. These molten Ni nanoparticles serve as catalysts for the graphitization of carbon, as discussed below. Subsequent to the formation of Ni nanoparticles, carbon and nitrogen deposit on these small metal nanoparticles, creating a solution of carbon and nitrogen within the molten nickel nanoparticles.[53] As carbon and nitrogen continue to deposit, they eventually form a saturated solution. At this temperature, as the reaction proceeds over time, the small molten particles coalesce, forming larger particles through a process similar to Ostwald ripening.[54,55] As more N and C vapor deposit on the small nanoparticles, the precipitation process leads to the formation of nucleation of ordered carbon frameworks, such as carbon nanotubes (CNTs)[38] or carbon globules,[56] depending on the size of the Ni nanoparticles. The medium size particles, having dimensions closer to the diameter of the carbon nanotubes form CNTs, but the bigger and also smaller nanoparticles form carbon globules with graphitic covering.[12] Interestingly, in the XRD, Raman, and XPS results, we observed an increased amount of graphitized carbon as we increased the melamine precursor content from 100 mg for the Ni−N100 sample to 500 mg for the Ni−N500 sample,

https://doi.org/10.1021/acsanm.4c02278
ACS Appl. Nano Mater. XXXX, XXX, XXX−XXX

although all other experimental conditions are the same during synthesis. This aspect can be understood, as discussed below. It is known from the literature that the solubility of nitrogen in metallic melts decreases as the carbon content in the melt increases[57] and vice versa. This decline in solubility has significant implications for our samples. The increase in the content of melamine (the nitrogen precursor) implies that there will be the presence of nitrogen in the molten nickel nanoparticles, and this will lead to a decrease in the solubility limit of carbon in the melt. As the melamine precursor content for the synthesis of the samples increases from 100 mg for the Ni−N100 sample to 500 mg for the Ni−N500 sample, we expect a gradual decrease in the solubility limit for carbon in the molten nickel nanoparticles from Ni−N100 to Ni−N500 sample.[58] The decrease in the solubility limit would lead to an enhanced precipitation of carbon. This precipitated carbon is graphitized carbon covering the Ni nanoparticles observed in our samples. As there is enough and higher supply of carbon and nitrogen vapors to the catalytic Ni-catalyst particles in the CVD chamber, we expect enhanced precipitation and formation of more graphitized carbon in the Ni−N500 sample as compared to the Ni−N100 sample. During the graphitization along with carbon, nitrogen was also included in the graphitic carbon layer. This results in an increased amount of N-doping (defects) in the graphitized carbon layer of the metallic nickel particles from Ni−N100 to the Ni−N500 samples, as we use a higher amount of melamine. All our characterization results such as XRD, Raman, XPS, TGA, and UV vis−DRS support this aspect. This explanation is clearly in line with the observed enhancement in the amount of formation of graphitized carbon (and nitrogen) with the increase in melamine precursor during synthesis of samples.

As there is plenty of overhead supply of carbon and nitrogen vapors in the CVD reaction chamber, the Ni nanoparticles are not able to transform all the carbon vapor into the graphitic carbon, and hence, the extra carbon vapor generally deposits on the precipitated graphitic carbon as amorphous carbon deposits.[43,56,59] As the amount of carbon in the precursors gradually increases from the Ni−N100 sample to the Ni−N500 sample (as discussed Section S2 1.3.1 and Table S3), we expect a higher amount of total carbon content in the Ni−N500 sample, in comparison to the other samples. This observation is supporting the results discussed under TGA that the weight fraction of carbon in the Ni−N500 sample is higher than that of Ni−N250 and NiN100 samples (Figure 3b).

3. HYDROGEN EVOLUTION REACTION (HER)

The hydrogen evolution reaction (HER) activity of the synthesized Ni−NY samples was assessed by using linear sweep voltammetry (LSV) and electrochemical impedance spectroscopy (EIS). Through current density measurements (LSV), we calculated the overpotential and compared active sites on catalyst surfaces. LSV was also employed to assess the activation energy barrier from room temperature (RT) to 45 °C. EIS provided insights into the dynamic interaction between adsorbed species and the catalyst's surface at different frequencies. More details on LSV and EIS studies will be discussed in the coming sections.

3.1. Linear Sweep Voltammetry (LSV) Study. Ni−NY (Y = 100, 250, and 500) samples were studied for catalytic activity in the electrochemical HER using N_2-saturated aqueous 1 M KOH solution at 10 mV/s scan rate. According to the literature survey,[11,60] an electrocatalyst can be considered highly efficient if it achieves a current density (j) of 10 mA/cm^2 at a lower overpotential (η_j). Therefore, to achieve the best overpotential, various amounts of Ni−NY catalysts were drop-cast onto a glassy carbon (GC) electrode, and their influence on the HER current density was examined. The catalyst loading was optimized for Ni−N500 and LSV illustrated in Figure 4a,b. Comparing the polarization curves

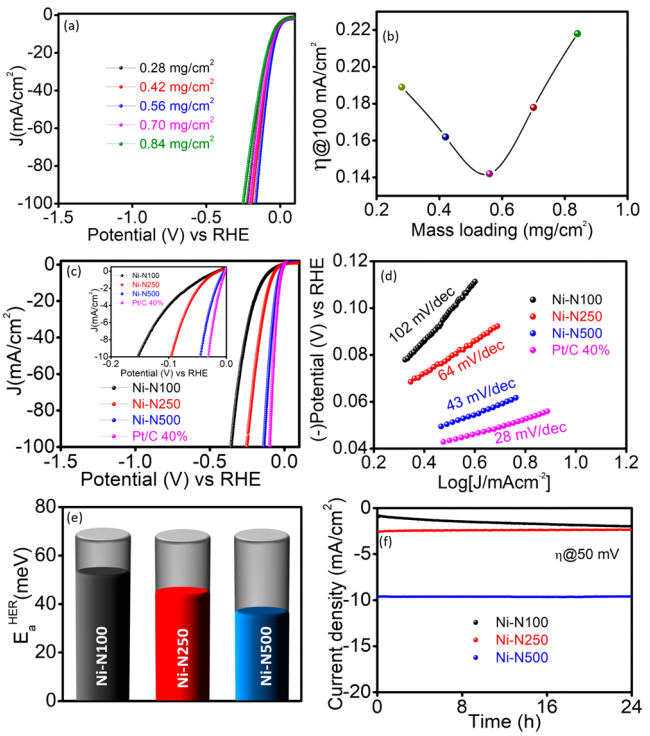

Figure 4. (a) HER−LSV polarization curve recorded on Ni−N500 at different mass loadings (0.28, 0.42, 0.56, 0.70, and 0.84 mg/cm^2) in N_2-saturated aqueous 1 M KOH solution with a scan rate of 10 mV/s. (b) Relation between η and mass loading. (c) HER−LSV curve recorded on Ni−NY (Y= 100, 250, and 500) and 40% Pt/C for comparative study. (d) Tafel plot. (e) The activation energy for HER at −0.2 V. (f) Chronoamperometry test at an applied overpotential of 50 mV for the stability of Ni−NY (Y = 100, 250, and 500) catalysts.

for different mass loadings, an increase in catalyst loading leads to a noticeable enhancement in the HER current density, reaching its maximum value at a mass loading of 0.56 mg/cm^2. We observed that a loading higher or lower than 0.56 mg/cm^2 increased the required overpotential. Figure 4b displays a correlation plot showing the relationship between overpotential (@100 mA/cm^2) and electrode mass loading (a thorough discussion on this aspect is detailed, Section S2 2.1). The highest current density and lowest overpotential were observed at a catalyst loading of 0.56 mg/cm^2. Therefore, this loading was chosen for subsequent electrochemical studies. In Figure 4c, it is noticed that at a loading of 0.56 mg/cm^2, the Ni−N500 sample exhibited an impressive performance with an overpotential of 45.6 mV at 10 mA/cm^2 (η_{10} = 45.6 mV), and with the same loading Pt/C 40% catalyst revealed 31.4 mV (η_{10} = 31.4 mV).

In order to discern the activity predominantly induced by N-doping, we assessed the LSV of the Ni−C sample (without N-doping) under identical experimental conditions. Furthermore, to discern the synergistic effects induced by nickel nanoparticles, we examined both reduced graphene oxide (rGO)

https://doi.org/10.1021/acsanm.4c02278
ACS Appl. Nano Mater. XXXX, XXX, XXX−XXX

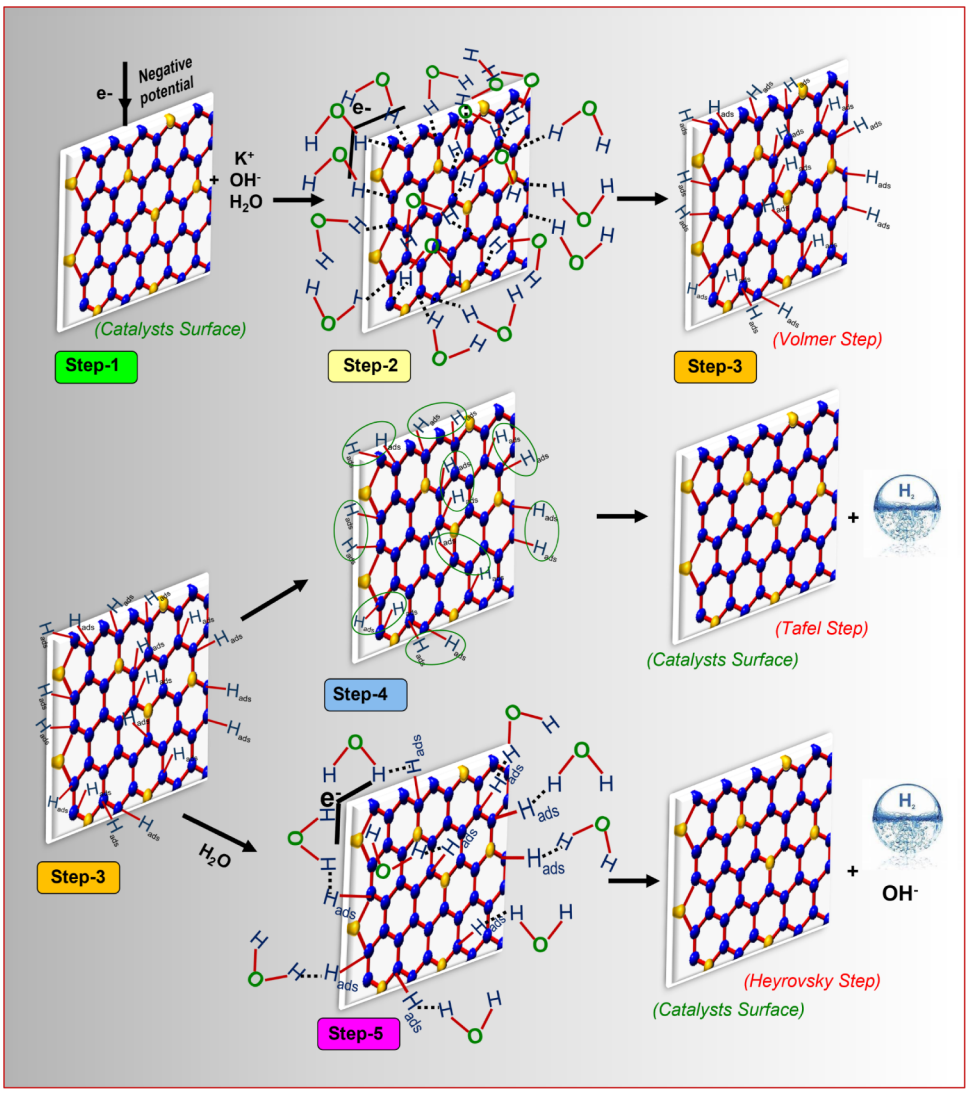

Figure 5. Reaction mechanism for HER kinetics on the outer surface of the catalysts.

and N-doped reduced graphene oxide (N-doped rGO), as shown in Figure S10. The LSV polarization curves (Figure S10a) distinctly illustrate that to achieve a current density of 10 mA/cm^2, rGO displays an overpotential of 1140 mV, which is reduced to 831 mV by N-doping (N-doped rGO): a significant improvement. Further improvement in overpotential is observed for the Ni−C sample, resulting in a reduced value of 480 mV. This overpotential of the Ni−C sample was further observed to be reduced by using varying concentrations of nitrogen dopant, i.e., Ni−NY samples. Consequently, the nickel nanoparticle-embedded carbon framework with the increased amount of nitrogen doping demonstrates a reduced overpotential compared to rGO, N-doped rGO, and Ni−C samples. It is noteworthy that Ni−N500 demonstrated superior cathodic current density and exhibited the lowest overpotential compared to Ni−N100 (η_{10} = 152.7 mV) and Ni−N250 (η_{10} = 91.1 mV) samples, as can be seen clearly in zoomed view of inset of Figure 4c. Table S6 compares the overpotential of Ni−NY samples and those of previously reported nickel-based electrocatalysts. Clearly, our sample requires a much lower overpotential than other reported ones, signifying the superiority of our samples.

Earlier, it was observed that the Pt electrode dissolves from the counter electrode to the acidic electrolytic medium and deposits on the working electrode, thereby leading to a better catalytic performance. Although, we have used basic medium, to avoid any kind of ambiguity on the dissolution of Pt in the electrolyte, and affecting the electrocatalytic activity, we repeated the LSV measurements using a graphite rod as the counter electrode and presented the results in Figure S11. The results indicate that the overpotential was found to be shifted merely 2.7 mV higher for Ni−NY samples and 3.4 mV higher for Pt/C, which is insignificant. Thus, the excellent performance of our samples is attributed to their intrinsic properties, which are unaffected by any dissolution of Pt.[61] Studies show that the active electrochemical surface area (ECSA) is directly proportional to the number of active centers in an electrocatalyst.[62] To determine this, cyclic voltammetry curves were recorded at different scans (Figure S12a−d) to estimate the double-layer capacitance (C_{dl}) (Figure S12e). The ECSA was then calculated by dividing the obtained C_{dl} by the specific capacitance (0.04 mF/cm^2).[31,63−65] The evaluated ECSA (Figure S12f) shows that Ni−NC500 has the highest number of active centers accessible for the hydrogen evolution reaction at 136.9 cm^2, significantly more than Ni−N100 (20 cm^2) and

https://doi.org/10.1021/acsanm.4c02278
ACS Appl. Nano Mater. XXXX, XXX, XXX−XXX

Ni−N250 (70.4 cm^2), while Pt/C has 248.1 cm^2. To validate the current density observed by LSV curves, rather than continuously recording the current, we sampled the current for 10 s at the applied potential values of −10, −20, −30, −40, −50, −60, and −70 mV (Figure S13). The results indicate that at each applied potential, the current remains constant over time and follows a pattern similar to the LSV results.

3.1.1. Explanation of Interfacial Electrode−Electrolyte Interaction for HER. To acquire crucial insights into the interaction between the electrode and the electrolyte, we depicted a schematic representation (Figure 5) of the various stages occurring during the linear sweep voltammetry experiment. As depicted in Figure 4c, the potential was initiated at +0.1 V versus the reversible hydrogen electrode (RHE), where the surface experienced the adsorption of OH^- ions due to electrostatic forces. The OH^- ions were desorbed from the surface as the potential gradually decreased below 0.0 V (negative potential). Consequently, hydrogen evolution occurred because of water (H_2O) splitting at the surface. It should be noted that there is a possibility of K^+ ions adhering to the electrode surface at negative potentials. However, due to steric hindrance from water molecules, the K^+ ions are prevented from adhering to the working electrode surface. Moreover, the reduction potential of K^+ is sufficiently high (−2.92 V), preventing its reduction. In the overall process, the following steps are involved in the reaction:

Step-1 (initial condition). No potential is applied yet; hence, all of the ions (K^+, OH^-, and H_2O) are homogeneously distributed throughout the solution.

Step-2 (adsorption of H_2O). As the potential gradually decreases, the surface of the catalysts adsorbs H_2O while simultaneously pushing out OH^- ions. This adsorption of H_2O primarily occurs at the carbon sites adjacent to the doped nitrogen atoms, which are more electron dense in nature. This process is illustrated in Figure 5, specifically depicted as step 2.

Step-3 (removal of OH^- ions from H_2O). Following the adsorption of H_2O, as the applied negative potential increases, some of the H atoms in contact with the C atoms of the catalyst split out from oxygen (of H_2O) and remain as adsorbed hydrogen (H_{ads}). The process of the generation of H_{ads} is facilitated by the electric field at the C atom along with the energetics of neighboring doped atoms. This step of the reaction is commonly known as the Volmer step and is represented by the following equation, where "S" indicates the active center (especially C next to the N atom):

$$S + H_2O + e^- \rightarrow S\text{-}H_{ads} + OH^- \text{(Volmer step)}$$

This process of adsorption of primary hydrogen (H_{ads}) occurs probabilistically equally at all of the active C sites simultaneously. Additionally, there is a possibility for the adsorption of hydrogen from adjacent H_2O molecules onto the adsorbed hydrogen atoms. However, this secondary process is less likely compared to the primary adsorption discussed in step 3.

Step-4. Gradually decreasing the potential, the adsorbed hydrogen atoms (which had been favorably adsorbed from H_2O) become unstable and start detaching from the surface. This detachment brings two nearby hydrogen atoms closer and forms the gaseous hydrogen, which leaves out the surface. This step of the reaction is known as the Tafel step.

$$S\text{-}H_{ads} + S\text{-}H_{ads} \rightarrow S + H_2 \uparrow \text{(Tafel step)}$$

Step-5. In case where adhesion is strong, direct detachment of hydrogen, as observed in step 4, may not occur. Instead, the HER can use a higher energy pathway. This variation arises from the varying strength of the hydrogen adsorption on different materials (electrodes). As the applied potential decreases, H_2O molecules gracefully align themselves toward the electrode, finding solace in the embrace of adsorbed hydrogen.

Consequently, the electrostatic force between H_{ads} and the oriented H_2O molecule intensifies with diminishing potential. The force is strong enough that we guess that the hydrogen from H_2O breaks at a faster rate than that of surface-to-adsorbed hydrogen (H_{ads}). These two hydrogen entities, H_{ads} and H (from H_2O), get closer and generate molecular or gaseous hydrogen, which gracefully departs from the catalyst's surface. This remarkable stage of the reaction is known as the Heyrovsky step.

$$S\text{-}H_{ads} + H_2O + e^- \rightarrow S + H_2 \uparrow + OH^- \text{(Heyrovsky step)}$$

3.1.2. Tafel Plot Analysis. The Tafel plot reveals mechanistic insights into electrode kinetics by plotting log J vs potential, utilizing the equation $\eta = b \log J + a$, where "b" represents the Tafel slope, and "a" represents the intercepts. Tafel slopes, $b = 2.303\ RT/\alpha F$ and $a = 2.303RT/\alpha F \log J_0$, where J_o represents the current exchange density, F represents the Faraday constant, R represents the gas constant, T represents the temperature, and α denotes the charge transfer coefficient. The obtained Tafel slope is associated with the rate-limiting step for HER. Volmer, Heyrovsky, and Tafel reaction steps correspond to Tafel slopes of 120, 40, and 30 mV/dec, respectively.[66] The Tafel slope value for Ni−N500 obtained 43 mV/dec at a lower overpotential correlates with many active sites available over Ni−N100 and Ni−N250 for 102 and 64 mV/dec, respectively, as shown in Table 1. The

Table 1. Overpotentials, Tafel Slopes, and Current Exchange Densities Were Obtained for Ni−NY (Y= 100, 250, and 500) Catalysts and the Reference, Pt/C 40% Catalyst, as Extracted from Figure 4

electrocatalysts	$\eta_{@10\ mAcm^{-2}}$(mV)	Tafel slope (mV dec^{-1})	J_0($mAcm^{-2}$)
Ni−N100	152.7	102	0.281
Ni−N250	91.1	64	0.363
Ni−N500	45.6	43	0.501
Pt/C 40%	31.4	28	0.691

Tafel slope values for these configurations are markedly lower than those for rGO, N-doped rGO, and Ni−C samples, which are 701, 638, and 127 mV/dec, respectively, as shown in Figure S10b. As a result, all Tafel slopes obtained on Ni−NY (Y= 100, 250, and 500) fall in the 40−120 mV/dec range, representing the HER mechanism is followed by Volmer−Heyrovsky pathways, and the rate-limiting step is governed by the Heyrovsky step.[67,68] Extrapolating the slopes on the x-axis allows for the extraction of another parameter known as the exchange current density, which plays a significant role in the catalytic performance. This suggests that as the exchange current density increases, the charge transfer kinetics increases.[69,70] From the overhead viewpoint, Ni−N500 shows the superior J_0 (0.501 mA/cm^2) as compared to Ni−N100 (J_0 = 0.281 mA/cm^2) and Ni−N250 (J_0= 0.363 mA/cm^2), generating the molecular (or gaseous) hydrogen and exiting the surface of catalysts quickly. The exchange current

https://doi.org/10.1021/acsanm.4c02278
ACS Appl. Nano Mater. XXXX, XXX, XXX−XXX

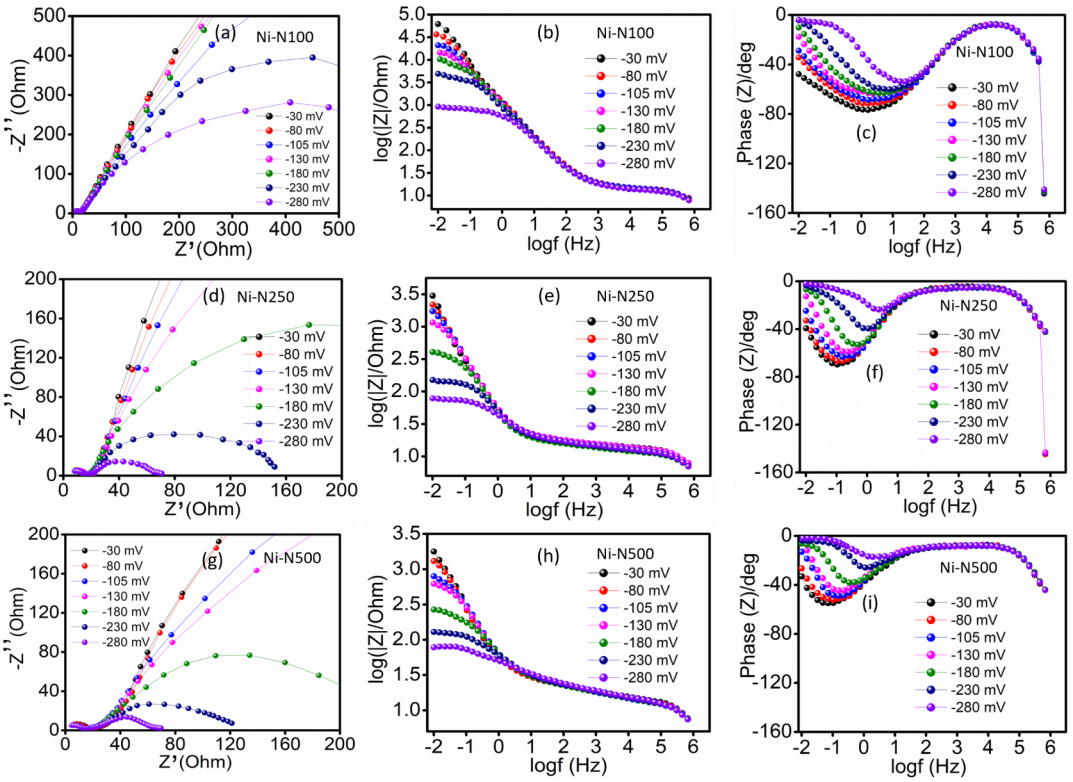

Figure 6. (a), (b), and (c) show the Nyquist, Bode magnitude, and Bode phase plots for the Ni−N100 sample, respectively. (d), (e), and (f) show Nyquist, Bode magnitude, and Bode phase plots for Ni−N250 sample, respectively. (g), (h), and (i) show the Nyquist, Bode magnitude, and Bode phase plots for the Ni−N500 sample, respectively.

density values surpass those of rGO, N-doped rGO, and Ni−C samples, measuring 0.134, 0.191, and 0.234 mA/cm^2, respectively.

Nitrogen insertion replaces C atoms with N atoms, gradually breaking the lattice structure and creating C vacancies. Further, the increased N content again stimulates the departure of C atoms in the framework.[71] The loss of C atoms creates defect sites, increasing the porosity and surface area. The induced nitrogen in C matrix changes in bond lengths alter electron density at neighboring carbon atoms, creating energetic electrochemical centers.[72] Overall, the deficiency of C atoms and N insertion reduces the H_2O adsorption energy, which further decreases with higher N content. The high I_{D1}/I_G ratio and large fwhm of C 1s (Figure S7b) indicate that the defects are mainly concentrated in the graphitic carbon plane for the Ni−N500 sample. These defects create a larger surface area, make more active sites for the electrochemical reactions to occur, and provide improved accessibility for water molecules to reach the active sites on the surface.[73] Therefore, the Ni−N500 sample with a higher defect concentration exhibits a greater specific surface area (246.9 m^2 g^{-1}) and pore size (5.365 nm) and shows reduced overpotential.

The knowledge of activation energy (E_a) is crucial for understanding a catalyst, as it provides insights into the reaction mechanism and the energy barriers involved.[74] The evaluation of the temperature dependence rate of the reaction allowed for the determination of the activation energy (further details are discussed in detail, Section S2 2.2 and Figure S14). The Ni−N500 catalyst shows the lowest activation energy (E_a) of 36.8 meV at −0.100 V vs RHE, indicating faster kinetics compared to Ni−N100 (53.3 meV) and Ni−N250 (47.7 meV), as displayed in Figure 4e. The nitrogen-doped carbon heterostructure altered electron delocalization and improved the surface energy. Subsequent improvement is made by wrapping on nickel nanoparticles, which changes the physical and chemical properties through a synergistic effect.[75] The altered surface energy facilitates the adsorption of H_2O on active sites, thereby promoting the HER. The stability of the catalysts holds immense significance. The long-term performance and durability of the catalysts directly impact their practical applicability and prevent degradation or surface restructuring. The chronoamperometry measurement was performed at an overpotential of 50 mV on the Ni−NY (Y = 100, 250, and 500) catalyst, as illustrated in Figure 4f. The Ni−N100 sample exhibited a stability decrease of approximately 30%, whereas both the Ni−N250 and Ni−N500 samples showed negligible stability decline over the course of 24 h. To validate the durability of the catalysts, the LSV polarization curves were recorded for multiple cycles. Specifically, the 10th and 2000th cycles were examined for each catalyst (Figure S15a-c). The results indicate that all catalysts exhibited a relatively small decrease in current density of approximately ∼6−8% after 2000 cycles. These findings suggest that the Ni−N500 catalyst exhibits better stability over multiple cycles in the HER process compared to the Ni−N100 and Ni−N250 catalysts.

3.2. Electrochemical Impedance (EIS) Analysis. EIS is a critical technique for investigating the property of the samples used on the electrode. Impedance, comprising resistance and capacitance, controls the current flow in a circuit. Plotting impedance against frequency (10 mHz − 1 MHz) reveals frequency-dependent variations. The response of ions with the applied frequency of impedance helps us to obtain the characteristic parameters at the interface of an electrochemical

https://doi.org/10.1021/acsanm.4c02278
ACS Appl. Nano Mater. XXXX, XXX, XXX−XXX

system. At the interface, the Nyquist plot of the impedance consists of a real part Z′ (ω) and imaginary part Z″ (ω), while the Bode plot consists of the absolute impedance (|Z|) or phase angle plotted as a function of frequency. The comprehensive study is outlined below.

3.2.1. EIS at Different Applied Potentials. The voltage at the electrode−electrolyte interface has a profound effect on charge dynamics. The EIS measurement is employed at various HER potential ranges to acquire a better understanding of the activity on Ni−NY samples (Figure 6). Figure 6a depicts a Nyquist plot recorded on catalyst Ni−N100 at potentials of −30, −80, −105, −130, −180, −230, and −280 mV, respectively, with a sinusoidal amplitude of 5 mV. The intermediate frequency range is associated with the Volmer step for hydrogen adsorption. In contrast, the high frequency (HF) region reflects the porosity and charge transfer resistance (R_{ct}), whereas the low frequency (LF) region corresponds to mass transfer.[76,77] The spectrum shows the linear behavior (at −30 mV) mainly due to a double layer of nearly pure capacitance, and deviation begins because the rate of adsorption of H_2O varies with the applied potential. Increasing potential (negative direction) reduces semicircle diameter in LF, while HF radius decrease enhances hydrogen production. The LF region is strongly dependent on potential; as it rises, the charged species and electron migration facilitate the kinetics at the interface and increase the reaction rate.[78] Comparing all the synthesized samples with increasing N content, we observed a decrease in the diameter of the semicircle (Figure 6a,d, and g) at all the applied potentials. The Ni−N500 sample contains a larger specific surface area, high pore volume, and a huge amount of defects. Therefore (in the LF region), it easily allows water molecules to diffuse inside the pores and to generate the charged species (OH^- ions). Nanocrystallites with porous structures and large surface areas enhance electrocatalytic activity, resulting in greater hydrogen evolution compared to smooth electrodes.

Figure 6b,e, and h show the Bode magnitude plots for Ni−N100, Ni−N250, and Ni−N500 samples, respectively. In the LF region, one could notice that the magnitude of impedance ($|Z|_{imp}$) is the highest (at −30 mV) for all of the samples. This may be due to the ions in the electrolyte, and the ions generated due to the splitting of H_2O molecules on the electrode surface are inhibited from diffusing further inside the electrode material. Thus, the response ($|Z|_{imp}$) of the ions is highly influenced by diffusion in the material. This is due to the ions following the applied oscillating field and favor diffusion into the electrode material, as described in the $|Z|_{imp}$ formulation(Section S2 2.3). Increasing the negative potential (from −30 mV to −280 mV) causes impedance values to decrease and curves to flatten in the LF region. With higher negative potential, even strongly adhered ions on the electrode surface start responding. Hence, the $|Z|_{imp}$ decreases with increasing negative potential. Simultaneously, the diffusional motions of the ions gradually increase, but the ions respond to a broad range of oscillating frequencies, which flattens/broadens the $|Z|_{imp}$ over this range of frequencies (further detailed information is available in Supporting Information, Section S2 2.4a). Any particular sample at a fixed applied potential may recognize three critical regions of $|Z|_{imp}$. They are (i) a flat region followed by a sharp decrease of $|Z|_{imp}$ in the LF region, (ii) A nearly flat region in the intermediate frequencies, and (iii) a gradual decrease of $|Z|_{imp}$ in the HF region. All Ni−NY samples in the LF region clearly observed an initial flat region, followed by a sharp decrease in $|Z|_{imp}$ with respect to the frequency. To understand the origin of the initial flat region, we consider the expression for the magnitude of impedance as shown in eq 1:[79]

$$|Z|_{imp} = \sqrt{ZZ^*} = \sqrt{R^2 + \frac{1}{(\omega C)^2}} = \sqrt{R^2 + X_C^2} \quad (1)$$

where all the symbols have their usual meaning. The observation of an almost constant $|Z|_{imp}$ over a range of frequencies implies that the terms in this equation, i.e., the resistance (R) and the capacitive reactance ($1/\omega C$), must be constant. In general, the value of R for any sample is constant (at a specific temperature). Hence, to attain a constant value of $|Z|_{imp}$, the capacitance must decrease continuously for a continuous increase in the frequency. The OH^- ions generated through the breakdown of H_2O commence diffusional motion at a particular applied voltage (further details are provided in Supporting Information, Section S2 2.4b). Here, the interesting observation is that the frequency range of the initial flat region increases with an increase in applied potential. Specifically, the Ni−N100 sample, characterized by smaller pores, exhibits a flat $|Z|_{imp}$ nature across a broad frequency range (Figure 6b), contrasting with the Ni−N250 and Ni−N500 samples, which possess larger pores, as depicted in Figure 6e,h, respectively. As it may be expected that the ions in the pores of higher pore size (diameter) can move quickly against steric hindrance, the capacitance diminishes sharply, and $|Z|_{imp}$ decreases faster in a short frequency range. Therefore, the slope of $|Z|_{imp}$ for the Ni−N100 sample decreases more slowly than that for Ni−N250 and Ni−N250 samples with frequency. This can be due to the capacitance growing slowly (further details are provided in Supporting Information, Section 2.2.4c).

All Ni−NY samples in the intermediate frequency range (from 10 Hz to 0.1 MHz) have an almost flat nature of $|Z|_{imp}$. For a nearly constant value of $|Z|_{imp}$, the capacitance term must constantly decrease as the frequency increases (eq 1). The following concept can be used to visualize the dynamics of ions. With increasing frequency, the amplitude of OH^- ion oscillation gradually decreases, limiting its diffusion within the electrode material. This could be because the velocity of the ions is slower than the fluctuation of the oscillating applied voltage. As a result, a slow reduction was observed in $|Z|_{imp}$. When comparing the $|Z|_{imp}$ across all Ni−NY samples, it is obvious that the frequency range exhibiting this intermediate zone of gradual reduction in $|Z|_{imp}$ is closely related to the amount and size of pores present in the samples (Figure 3d). Filipe et al.[80] investigated the charging dynamics inside arbitrary-sized cylindrical pores, demonstrating that the charge stored per unit volume of the pore (volumetric capacitance) diminishes as relative pore size increases (further aspects are discussed in Supporting Information, Section S2 2.4d). As previously stated, the Ni−N500 sample has the greatest pore volume for all pore sizes among the as-synthesized samples. Many larger-sized pores contribute to higher effective capacitance, resulting in higher $|Z|_{imp}$ for the sample. Simultaneously, as the mean pore size increases for the Ni−N500 sample, the corresponding capacitance decreases, while the $|Z|_{imp}$ increases (Figure 6be, and h).

Beyond 0.1 MHz, i.e., $\log f \geq 5$, all Ni−NY samples exhibit a progressive decrease in $|Z|_{imp}$. This could be ascribed to a decrease in the OH^- ion oscillation amplitude. The amplitude

https://doi.org/10.1021/acsanm.4c02278
ACS Appl. Nano Mater. XXXX, XXX, XXX−XXX

of the oscillation appears to be so modest that the ions oscillate at their positions without disrupting the neighboring ions. As a result, the impedance aggressively drops, as measured with instrumental restrictions of up to 1.0 MHz.

From the concept of AC theory, in the case of an ideal capacitor, the response current lags the applied voltage by 90° in phase. The Bode phase plot for Ni−NY samples recorded at different potentials of −30, −80, −105, −130, −180, −230, and −280 mV is shown in Figure 6c,f, and i for Ni−N100, Ni−N250, and Ni−N500 samples, respectively. A phase lag (negative phase) was observed, indicating that carbonaceous substances are electrically insulating in nature. The Ni−N100 sample exhibits phase lag of −48° at 10 mHz ($\log f = -2$) for the applied voltage of −30 mV (Figure 6c). As previously noted, the electrolyte species are partially permeated (diffusion) into the carbonaceous electrode, which becomes adsorbed there. Because of this adsorption, the motion of the charged species is hindered, and they do not follow the field, resulting in a phase lag of −48° at 10 mHz. However, as the applied potential gradually increases toward a value of −280 mV, the adsorption strength (between the ions and the active carbon centers) decreases, and the mobility of the electrolyte species increases. This allows a gradual decrease in phase lagging in the very LF region ($\log f = -2$), which is displayed in Figure 6f,i), as will be discussed later. The increasing frequency of the oscillating field leads to a gradual phase lag of ions generated in the sample's pores due to electrostatic force and steric hindrance. This increases the phase difference between the oscillating potential and current-generating species. A maximum phase difference of −77° for the Ni−N100 sample is observed at a frequency of 1.3 Hz for an applied potential of −30 mV. The porous nature of the samples, with its distribution of electrostatic forces and steric hindrances, may limit the maximum phase difference. Pores and surface features enable diffusive ion motion based on pore size (further information is discussed in detail in Supporting Information, Section S2 2.4e).

As the potential amplitude gradually increases from −30 to −280 mV, the generation of ions, especially OH^- ions, increases due to the catalytic process at active sites. However, the ion generation rate and response vary with the oscillating potential. In the presence of rising frequency, the oscillating OH^- ions obstruct the creation of new charges, resulting in an increasing phase difference ranging from ∼0° to ∼−90° (further details are discussed in Supporting Information, Section S2 2.4f). The phase lag rapidly diminishes and reaches zero as the frequency increases beyond 1.3 Hz. This behavior is expected due to the contact period (interaction time) between ions and oscillating potential diminishes. The sample's pore volume and size determine the phase lag. The electrode material exhibits an opposing polarization oscillation at higher frequencies, resulting in a rapid phase drop to ∼−180°. This behavior is consistent with prior observations and emphasizes the complicated dynamics of ion response to different frequencies and polarization[8] (further details are provided in Supporting Information, Section S2.2.4g).

A comparison of the Bode phase plots at fixed frequencies and potentials reveals a drop in phase from Ni−N100 to Ni−N500 samples (Figure 6c,f, and i). The observed reduction in phase could be attributed to the Ni−N500 sample's bigger pore capacity and higher surface area, which allows easier diffusion with lower obstruction. The maximum phase angle of the Ni−N500 sample rapidly changes as the voltage increases, suggesting effective diffusion through the carbon layer toward the inner carbon layer of the metallic electrode surface. The Ni−N100 sample has the most remarkable phase difference at 10 kHz with the smallest pore volume, whereas the Ni−N250 sample has the smaller phase due to larger pores. As a result, the sequence of phase differences at 10 kHz is Ni−N100 > Ni−N500 > Ni−N250 (these aspects are discussed in detail in Supporting Information, Section S2.2.4h).

3.2.2. Discussion on the EIS Behavior of the Catalysts at a Fixed Potential. To examine the interfacial activity of the catalysts, EIS is conducted in a 1 M KOH solution at an applied potential of −230 mV. The potential (−230 mV) is chosen such that LSV (Figure 4c) results indicate an efficient hydrogen evolution reaction. It engaged the equivalent circuit (Figure 7a) to fit the Nyquist plots (Figure 7b), and the resulting parameters are presented in Table S2. The connection of elements in the circuit is explained, Section 2.2.5a. The Nyquist plot shows two semicircles representing different phenomena: the first at a higher frequency signifies porosity, and the second at a lower frequency represents the charge transfer mechanism in HER.[81,82] Two constant phase elements (Q_{dl} and Q_{ads}) are used due to the porous heterostructures electrode. The carbon matrix in our samples is modified with various nitrogen concentrations (2.3%, 4.5%, and 7.2% for Ni−N100, Ni−N250, and Ni−N500, respectively). This modification creates defects and pores in the carbon network, increasing the surface reactivity of the electrode. These varying-diameter pores allow charges to move via different resistance. The kinetic parameters (R_{ct} and R_{ads}) decrease with increasing nitrogen content in the catalyst, as indicated in the inset of Figure 7b and Table 2. This shows the depressed semicircle (LF region), which suggests ion diffusion as the pore size increases in the materials.

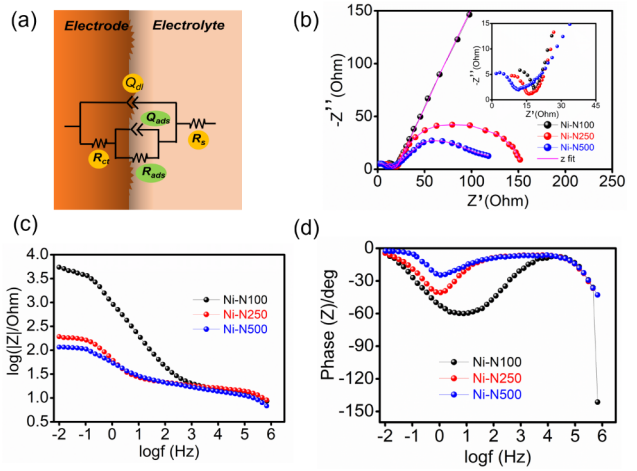

Figure 7. (a) Schematic of the Randle equivalent circuit at the interface, (b) Nyquist plot, (c) Bode magnitude, and (d) Bode phase plots in the frequency range from 10 mHz to 1 MHz at an applied potential of −230 mV for Ni−N100, Ni−N250, and Ni−N500 samples, recorded in the aqueous 1 M KOH solution.

Figure 7c shows a comparison of the Bode magnitude plots (log(|Z|) vs log(f)) of Ni−NY samples reported at a potential of −230 mV. The Ni−N100 sample exhibits the highest $|Z|_{imp}$ value in the low-frequency range. As discussed earlier, smaller pores have more capacity to store the charge (capacitance) than bigger pores; therefore, larger pores significantly reduce

https://doi.org/10.1021/acsanm.4c02278
ACS Appl. Nano Mater. XXXX, XXX, XXX−XXX

Table 2. Electrochemical Impedance Data Recorded on Ni−NY (Y = 100, 250, and 500) at −230 mV Potential in 1 M KOH Solution Over the Frequency Range 10 mHz−1 MHz

electrocatalysts	$R_{ct}(\Omega)$	$R_{ads}(\Omega)$	$Q_{dl}(\mu\Omega^{-1}s^{n}cm^{-2})$	$Q_{ads}(m\Omega^{-1}s^{n}cm^{-2})$
Ni−N100	15.1	1180	209.1	0.312
Ni−N250	14.8	152	232.2	7.5
Ni−N500	12.1	135	586.3	147.3

average impedance. This could explain the reason for the Ni−N100 sample, which has a greater $|Z|_{imp}$ value at constant frequency due to fewer bigger pores (Figure 3d). Furthermore, as the frequency increases, the impedance magnitude gradually lowers until it achieves a constant value at intermediate frequencies. This behavior can be explained using eq 1. The observed differences in impedance drop rates in the samples are attributed to variations in capacitance, which is related to pore sizes and distribution (Figure S4). The Ni−N100 sample exhibits a slower reduction of impedance due to a higher volume of smaller pores and lower volume of bigger pores (these aspects are further discussed in detail in Supporting Information, Section S2 2.5b). In contrast, the Ni−N500 sample, composed of highly defective graphitic carbon, allows for easy ion diffusion, resulting in a smoother response over a narrow impedance range. The ions experience limited physical motion at higher frequencies and do not respond to the applied field. These findings suggest the consequence of pore size and distribution on the impedance behavior throughout the frequency ranges.

Figure 7d depicts the Bode phase plots for Ni−NY samples at the applied potential of −230 mV. As the nitrogen content in the graphitic layer increases, the maxima of the phase angle shift to lower phase angles at lower frequencies. If the charged species have enough time in the LF region, the highly porous (larger pore size) carbonaceous electrode (Ni−N500 sample, 7.2% N) allows diffusion. In this scenario, the ions nearly follow the applied potential field and exhibit the minimum phase angle. In the same fashion, a minimum phase of −24.3° was observed for the Ni−N500 sample.[8,10] The Ni−N100 sample, with a lower nitrogen content, features a densely packed N-doped graphitic carbon layer that inhibits electron conduction. This dense structure increases resistance (impedance) due to steric hindrance within smaller pores, thereby influencing diffusion processes. As a result, large phase differences of −40° and −60° were reported for Ni−N250 and Ni−N100 samples, respectively.

3.3. Postmortem Analysis of Ni−NY (Y = 100, 250, and 500) Samples after HER. The exceptional catalytic performance of Ni−NY samples prompted us to investigate whether our catalysts retained their properties. We studied the catalysts using XRD, Raman, SEM, and TEM for this purpose. The XRD patterns of the Ni−N100, Ni−N250, and Ni−N500 catalysts before and after the electrochemical studies are depicted in Figure 8a,b, respectively. The XRD patterns of the catalysts after electrochemical experiments showed the development of an additional peak at 19.7°, which could be attributed to the presence of a trace amount of $Ni(OH)_2$. We observed that, there is an insignificant growth of $Ni(OH)_2$ in the alkaline media, which is not able to make any structural distortion, therefore, the catalysts stay stable and are unaffected during the LSV measurements, proving their practical stability of samples. The Raman spectra investigation revealed a decrease in the intensity and sharpness of the D band in the

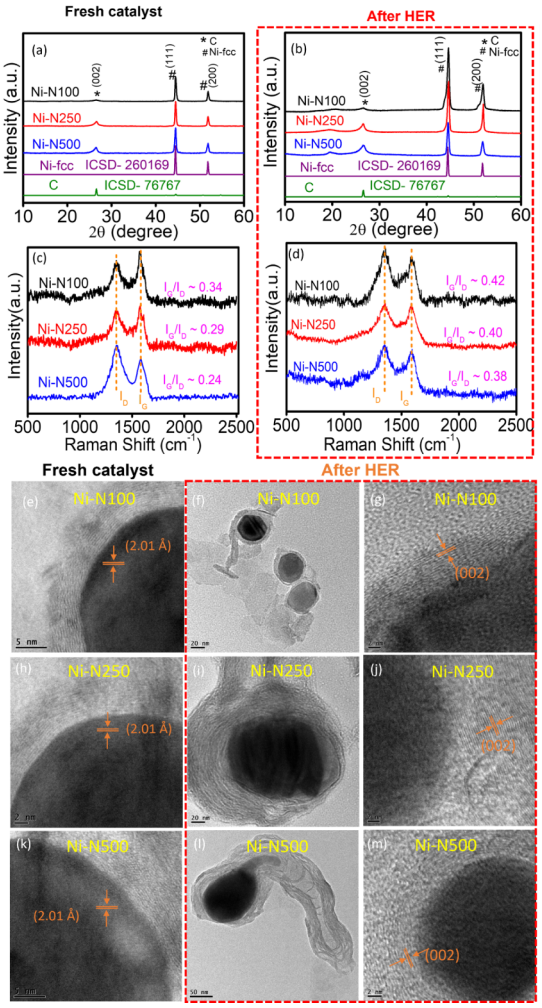

Figure 8. (a) XRD patterns and (c) Raman spectra before electrocatalysis, while (b) shows XRD patterns and (d) shows Raman spectra of Ni−NY (Y = 100, 250, and 500) after HER measurement. (e), (h), and (k) HRTEM images of fresh catalysts for Ni−N100, Ni−N100, and Ni−N500, respectively (Left Panel). (f), (i), and (l) Bright-field low-magnification TEM image (Middle Panel), and (g), (j), and (m) HRTEM images of Ni−N100, Ni−N100, and Ni−N500, respectively, after HER catalysis (Right Panel).

catalysts following the HER measurements, indicating reduced graphitization (Figure 8c,d). Additionally, a higher intensity of the D3 peak was found using the least-squares fitting of the Raman spectra, as depicted in Figure S16. The increased intensity indicates that the catalysts following the HER process are more amorphous. Furthermore, a slight boost in the intensity of the D4 peak is caused by the localization of the electron density in the structure. The entire Raman study demonstrates that the I_G/I_D ratio obtained following HER examination aligns with earlier findings, implying a consistent level of graphitization and highlighting the robust nature of the electrocatalysts.

Similarly, we also investigated electron microscopic analysis (i.e., SEM and TEM). The SEM image (Figure S17) demonstrates that carbon aggregates increase in size across all samples following HER testing, yet their shape remains unchanged. This suggests that all Ni−NY catalysts maintain a consistent nanostructure shape, as depicted in Figure S17. Furthermore, the TEM images of Ni−NY catalysts are displayed in Figure 8e-m. The Ni−N500 catalyst, reveals a

https://doi.org/10.1021/acsanm.4c02278
ACS Appl. Nano Mater. XXXX, XXX, XXX−XXX

similar morphology and retention of the covering of nickel nanoparticles through graphitic carbon layers, as shown in Figure 8l,m, respectively. This suggests that the degree of graphitization remains unaffected over the several cycles (2000 cycles) of LSV. Similarly, the Ni−N100 (Figure 8f,g) and Ni−N250 catalysts (Figure 8i,j), indicate that these catalysts have equivalent (after HER examination) properties to the fresh catalyst. As a result, the overall structural change on our Ni−NY (Y = 100, 250, and 500) was unaffected by the HER electrocatalysis measurement. All the studies show behavior similar to that of the fresh catalyst, confirming that the catalyst structurally remains unchanged following all the electrochemical studies. The results indicate that the catalysts remain stable with some insignificant structural changes. The stability is particularly pronounced in the Ni−N500 catalyst, which shows no graphitization changes. The findings collectively suggest that these catalysts are robust and can maintain their structural integrity under challenging electrochemical conditions, making them suitable for applications in catalysis.

4. CONCLUSION

In summary, we have approached a straightforward synthesis method for the nickel-embedded nitrogen-doped carbon matrix Ni−NY (Y = 100, 250, and 500). The experimental results imply that plentiful amount of electrochemically active sites are created spatially in tiny pores, particularly optimally in the Ni−N500 sample. The heterogeneity and defects created in the structure offer a better accessible and exposed active center, synchronizing the high catalytic activity and stability of catalysts via creating a localized electron density at the C atoms neighboring the N-centers. The HER activity was evidenced by minimum overpotential ($\eta_{10\ mA/cm^2}$ = 45.6 mV), lower Tafel slope (43 mV/dec), a sharp increase in current density, and lower activation energy (36.8 meV). The catalysts show good stability and durability under harsh electrochemical conditions. Furthermore, EIS is employed to elucidate the dynamics of charges at the interface under various applied potentials. Benefiting from the abundance of distributed pores (size and volume), the movement of charges encounters numerous resistance levels, thereby leading to alterations in the impedance ($|Z|_{imp}$). The pores of larger size in Ni−N500 sample contribute significantly to the reduction of average impedance. This phenomenon could potentially elucidate the reason behind the smaller $|Z|_{imp}$ value observed, particularly at a constant frequency. The overall structure of the catalysts offers enhanced electrochemically active sites, higher specific surface areas, and larger pores in the material. The catalyst's unique coalescence of nickel nanoparticles and nitrogen-doped carbon layer enables efficient hydrogen extraction from H_2O, positioning it as a promising replacement to conventional catalysts reliant on precious metals.

ASSOCIATED CONTENT

Supporting Information

The Supporting Information is available free of charge at https://pubs.acs.org/doi/10.1021/acsanm.4c02278.

Experimental section, XRD, Raman, and XPS fittings, SEM and SEM-EDX schematic, TEM image, N_2 adsorption/desorption BET for pore distribution, Urbach energy plot, LSV curves, Tafel plot, CV curves, and activation energy estimation (PDF)

AUTHOR INFORMATION

Corresponding Author

Balaram Sahoo − *Materials Research Centre, Indian Institute of Science, Bengaluru, Karnataka 560012, India;* orcid.org/0000-0002-2050-4746; Phone: +91-80-2293 2943; Email: bsahoo@iisc.ac.in

Authors

Sarvesh Kumar − *Materials Research Centre, Indian Institute of Science, Bengaluru, Karnataka 560012, India;* orcid.org/0000-0002-5457-3512

Rajeev Kumar − *Materials Research Centre, Indian Institute of Science, Bengaluru, Karnataka 560012, India;* orcid.org/0000-0002-5436-2352

Naveen Goyal − *Materials Research Centre, Indian Institute of Science, Bengaluru, Karnataka 560012, India;* orcid.org/0000-0002-8827-2646

Ankit Yadav − *Materials Research Centre, Indian Institute of Science, Bengaluru, Karnataka 560012, India;* orcid.org/0000-0002-2239-8000

Swetha BM − *Department of Mechanical Engineering, MS Ramaiah Institute of Technology, Bengaluru, Karnataka 560054, India*

Complete contact information is available at: https://pubs.acs.org/10.1021/acsanm.4c02278

Notes

The authors declare no competing financial interest.

ACKNOWLEDGMENTS

The authors acknowledge the Solid State and Structural Chemistry Unit, and the Inorganic and Physical Chemistry, IISc Bangalore, for providing the BET facility and the XPS facility, respectively. The authors are grateful to IISC's Advanced Facility for Microscopy and Microanalysis (AFMM) for providing the TEM facility.

REFERENCES

(1) Fei, H.; Yang, Y.; Peng, Z.; Ruan, G.; Zhong, Q.; Li, L.; Samuel, E. L. G.; Tour, J. M. Cobalt Nanoparticles Embedded in Nitrogen-Doped Carbon for the Hydrogen Evolution Reaction. *ACS Appl. Mater. Interfaces* **2015**, *7* (15), 8083−8087.

(2) Lv, X.; Ren, J.; Wang, Y.; Liu, Y.; Yuan, Z. Y. Well-Defined Phase-Controlled Cobalt Phosphide Nanoparticles Encapsulated in Nitrogen-Doped Graphitized Carbon Shell with Enhanced Electrocatalytic Activity for Hydrogen Evolution Reaction at All-PH. *ACS Sustainable Chem. Eng.* **2019**, *7* (9), 8993−9001.

(3) Liu, S.; Shen, Y.; Zhang, Y.; Cui, B.; Xi, S.; Zhang, J.; Xu, L.; Zhu, S.; Chen, Y.; Deng, Y.; Hu, W. Extreme Environmental Thermal Shock Induced Dislocation-Rich Pt Nanoparticles Boosting Hydrogen Evolution Reaction. *Adv. Mater.* **2022**, *34* (2), 2106973.

(4) Nazir, R.; Fageria, P.; Basu, M.; Pande, S. Decoration of Carbon Nitride Surface with Bimetallic Nanoparticles (Ag/Pt, Ag/Pd, and Ag/Au) via Galvanic Exchange for Hydrogen Evolution Reaction. *J. Phys. Chem. C* **2017**, *121* (36), 19548−19558.

(5) Popczun, E. J.; Read, C. G.; Roske, C. W.; Lewis, N. S.; Schaak, R. E. Highly Active Electrocatalysis of the Hydrogen Evolution Reaction by Cobalt Phosphide Nanoparticles. *Angew. Chem., Int. Ed.* **2014**, *53* (21), 5427−5430.

(6) Yusuf, B. A.; Xie, M.; Yaseen, W.; Xie, J.; Xu, Y. Simultaneous Fabrication of Cobalt-Based Graphene with Rich N Dopant for Hydrogen Evolution Reaction in Basic Medium. *Int. J. Energy Res.* **2021**, *45* (9), 14010−14020.

(7) Chen, Z.; Wu, R.; Liu, Y.; Ha, Y.; Guo, Y.; Sun, D.; Liu, M.; Fang, F. Ultrafine Co Nanoparticles Encapsulated in Carbon-

Nanotubes-Grafted Graphene Sheets as Advanced Electrocatalysts for the Hydrogen Evolution Reaction. *Adv. Mater.* **2018**, *30* (30), 1802011.
(8) Yadav, A.; Kumar, R.; Sahoo, B. Graphene Oxide Coatings on Amino Acid Modified Fe Surfaces for Corrosion Inhibition. *ACS Appl. Nano Mater.* **2020**, *3* (4), 3540−3557.
(9) Yadav, A.; Kumar, R.; Choudhary, H. K.; Sahoo, B. Graphene-Oxide Coating for Corrosion Protection of Iron Particles in Saline Water. *Carbon* **2018**, *140*, 477−487.
(10) Yadav, A.; Kumar, R.; Pandey, U. P.; Sahoo, B. Role of Oxygen Functionalities of GO in Corrosion Protection of Metallic Fe. *Carbon* **2021**, *173*, 350−363.
(11) Goyal, N.; Rai, R. K. *Recent Progress in the Synthesis and Electrocatalytic Application of Metal−Organic Frameworks Encapsulated Nanoparticle Composites BT - Metal-Organic Frameworks (MOFs) as Catalysts*, Gulati, S., Ed.; Springer Nature Singapore: Singapore, 2022; pp. 731764. DOI: .
(12) Kumar, R.; Kumar, A.; Verma, N.; Philip, R.; Sahoo, B. Mechanistic Insights into the Optical Limiting Performance of Carbonaceous Nanomaterials Embedded with Core-Shell Type Graphite Encapsulated Co Nanoparticles. *Phys. Chem. Chem. Phys.* **2020**, *22* (46), 27224−27240.
(13) Kumar, R.; Kumar, A.; Verma, N.; Philip, R.; Sahoo, B. FeCoCr Alloy-Nanoparticle Embedded Bamboo-Type Carbon Nanotubes for Non-Linear Optical Limiting Application. *J. Alloys Compd.* **2020**, *849*, 156665.
(14) Kumar, R.; Kumar, A.; Verma, N.; Khopkar, V.; Philip, R.; Sahoo, B. Ni Nanoparticles Coated with Nitrogen-Doped Carbon for Optical Limiting Applications. *ACS Appl. Nano Mater.* **2020**, *3* (9), 8618−8631.
(15) Wu, P.; Yu, S.; Liu, H.; Zhang, X.; Hou, L.; Niu, B.; Jiang, J.; Liu, S.; Fu, J. Nickel-Copper Alloy Nanoparticles Embedded in N-Doped Porous Carbon Nanosheets for Supercapacitors and Hydrogen Evolution Reaction. *ACS Appl. Nano Mater.* **2022**, *5* (7), 9447−9459.
(16) Ji, X.; Liu, B.; Ren, X.; Shi, X.; Asiri, A. M.; Sun, X. P-Doped Ag Nanoparticles Embedded in N-Doped Carbon Nanoflake: An Efficient Electrocatalyst for the Hydrogen Evolution Reaction. *ACS Sustainable Chem. Eng.* **2018**, *6* (4), 4499−4503.
(17) Ma, W.; Miao, M.; Han, G.; Wu, J.; Yu, X.; Zheng, J.; Jiang, S.; Han, Y. F.; Ma, R. Hierarchical Nickel Clusters Encapsulated in Ultrathin N-Doped Graphitic Nanocarbon Hybrids for Effective Hydrogen Evolution Reaction. *ACS Sustainable Chem. Eng.* **2019**, *7* (17), 15127−15136.
(18) Barman, B. K.; Nanda, K. K. CoFe Nanoalloys Encapsulated in N-Doped Graphene Layers as a Pt-Free Multifunctional Robust Catalyst: Elucidating the Role of Co-Alloying and N-Doping. *ACS Sustainable Chem. Eng.* **2018**, *6* (10), 12736−12745.
(19) Liu, X.; Sun, W.; Chen, J.; Wen, Z. Controllable Electrochemical Liberation of Hydrogen from Sodium Borohydride. *Angew. Chem., Int. Ed.* **2024**, *63*, No. e202317313.
(20) Logan, B. E.; Call, D.; Cheng, S.; Hamelers, H. V. M.; Sleutels, T. H. J. A.; Jeremiasse, A. W.; Rozendal, R. A. Microbial Electrolysis Cells for High Yield Hydrogen Gas Production from Organic Matter. *Environ. Sci. Technol.* **2008**, *42* (23), 8630−8640.
(21) Mondal, R.; Thimmappa, R.; Nayak, B.; Dewan, A.; Devendrachari, M. C.; Chen, Q.; Wen, Z.; Thotiyl, M. O. A Spontaneous Hydrogen Fuel Purifier under Truly Ambient Weather Conditions. *Energy Environ. Sci.* **2023**, *16* (9), 3860−3872.
(22) Browne, M. P.; Stafford, S.; O'Brien, M.; Nolan, H.; Berner, N. C.; Duesberg, G. S.; Colavita, P. E.; Lyons, M. E. G. The Goldilocks Electrolyte: Examining the Performance of Iron/Nickel Oxide Thin Films as Catalysts for Electrochemical Water Splitting in Various Aqueous NaOH Solutions. *J. Mater. Chem. A* **2016**, *4* (29), 11397−11407.
(23) Zhang, B.; Xiao, C.; Xie, S.; Liang, J.; Chen, X.; Tang, Y. Iron-Nickel Nitride Nanostructures in Situ Grown on Surface-Redox-Etching Nickel Foam: Efficient and Ultrasustainable Electrocatalysts for Overall Water Splitting. *Chem. Mater.* **2016**, *28* (19), 6934−6941.
(24) Devi, B.; Koner, R. R.; Halder, A. Ni(II)-Dimeric Complex-Derived Nitrogen-Doped Graphitized Carbon-Encapsulated Nickel Nanoparticles: Efficient Trifunctional Electrocatalyst for Oxygen Reduction Reaction, Oxygen Evolution Reaction, and Hydrogen Evolution Reaction. *ACS Sustainable Chem. Eng.* **2019**, *7* (2), 2187−2199.
(25) Li, S. T.; Shi, G. M.; Li, Q.; Shi, F. N.; Wang, X. L.; Yang, L. M. One-Step Synthesis and Performances of Ni@CN Nanocapsules with Superior Dual-Function as Electrocatalyst and Microwave Absorbent. *Colloids Surfaces A Physicochem. Eng. Asp.* **2021**, *615*, 126162.
(26) Yan, X.; Gu, M.; Wang, Y.; Xu, L.; Tang, Y.; Wu, R. In-Situ Growth of Ni Nanoparticle-Encapsulated N-Doped Carbon Nanotubes on Carbon Nanorods for Efficient Hydrogen Evolution Electrocatalysis. *Nano Res.* **2020**, *13* (4), 975−982.
(27) Lu, J.; Yin, S.; Shen, P. K. Carbon-Encapsulated Electrocatalysts for the Hydrogen Evolution Reaction. *Electrochem. Energy Rev.* **2019**, *2* (1), 105−127.
(28) Deng, H.; Li, Q.; Liu, J.; Wang, F. Active Sites for Oxygen Reduction Reaction on Nitrogen-Doped Carbon Nanotubes Derived from Polyaniline. *Carbon* **2017**, *112*, 219−229.
(29) Sheng, Z.-H.; Shao, L.; Chen, J. J.; Bao, W. J.; Wang, F. B.; Xia, X. H. Catalyst-Free Synthesis of Nitrogen-Doped Graphene via Thermal Annealing Graphite Oxide with Melamine and Its Excellent Electrocatalysis. *ACS Nano* **2011**, *5* (6), 4350−4358.
(30) Wu, D. H.; Ul Haq, M.; Zhang, L.; Feng, J. J.; Yang, F.; Wang, A. J. Noble Metal-Free FeCoNiMnV High Entropy Alloy Anchored on N-Doped Carbon Nanotubes with Prominent Activity and Durability for Oxygen Reduction and Zinc−Air Batteries. *J. Colloid Interface Sci.* **2024**, *662*, 149−159.
(31) Kumar, R.; Kumar, S.; Chandrappa, S. G.; Goyal, N.; Yadav, A.; Ravishankar, N.; Prakash, A. S.; Sahoo, B. Nitrogen-Doped Carbon Nanostructures Embedded with Fe-Co-Cr Alloy Based Nanoparticles as Robust Electrocatalysts for Zn-Air Batteries. *J. Alloys Compd.* **2024**, *984*, 173862.
(32) Cai, W.; Luo, X.; Jiang, Y.; Liu, Z.; Li, J.; Ma, L.; Xiong, J.; Yang, Z.; Cheng, H. Nitrogen-Doped Carbon Active Sites Boost the Ultra-Stable Hydrogen Evolution Reaction on Defect-Rich MoS_2 Nanosheets. *Int. J. Hydrogen Energy* **2018**, *43* (4), 2026−2033.
(33) Yang, G.; Han, H.; Li, T.; Du, C. Synthesis of Nitrogen-Doped Porous Graphitic Carbons Using Nano-$CaCO_3$ as Template, Graphitization Catalyst, and Activating Agent. *Carbon* **2012**, *50* (10), 3753−3765.
(34) Lu, T.; Chen, Q. A Simple Method of Identifying π Orbitals for Non-Planar Systems and a Protocol of Studying π Electronic Structure. *Theor. Chem. Acc.* **2020**, *139* (2), 25.
(35) Liu, Z.; Lu, T.; Chen, Q. An Sp-Hybridized All-Carboatomic Ring, Cyclo[18]Carbon: Bonding Character, Electron Delocalization, and Aromaticity. *Carbon* **2020**, *165*, 468−475.
(36) Blume, R.; Rosenthal, D.; Tessonnier, J. P.; Li, H.; Knop-Gericke, A.; Schlögl, R. Characterizing Graphitic Carbon with X-Ray Photoelectron Spectroscopy: A Step-by-Step Approach. *ChemCatchem* **2015**, *7* (18), 2871−2881.
(37) Nandan, R.; Devi, H. R.; Kumar, R.; Singh, A. K.; Srivastava, C.; Nanda, K. K. Inner Sphere Electron Transfer Promotion on Homogeneously Dispersed Fe-N_XCenters for Energy-Efficient Oxygen Reduction Reaction. *ACS Appl. Mater. Interfaces* **2020**, *12* (32), 36026−36039.
(38) Kumar, R.; Khan, M. A.; Anupama, A. V.; Krupanidhi, S. B.; Sahoo, B. Infrared Photodetectors Based on Multiwalled Carbon Nanotubes: Insights into the Effect of Nitrogen Doping. *Appl. Surf. Sci.* **2021**, *538*, 148187.
(39) Yadav, A.; Kumar, R.; Kumar, S.; Sahoo, B. Mechanistic Insights into the Roles of Precursor Content, Synthesis Time, and Dispersive Solvent in Maximizing Supercapacitance of N-RGO Sheets. *J. Alloys Compd.* **2024**, *971*, 172648.
(40) Zhu, J.; Holmen, A.; Chen, D. Carbon Nanomaterials in Catalysis: Proton Affinity, Chemical and Electronic Properties, and Their Catalytic Consequences. *ChemCatchem* **2013**, *5* (2), 378−401.

https://doi.org/10.1021/acsanm.4c02278
ACS Appl. Nano Mater. XXXX, XXX, XXX−XXX

(41) Zhu, Z. H.; Hatori, H.; Wang, S. B.; Lu, G. Q. Insights into Hydrogen Atom Adsorption on and the Electrochemical Properties of Nitrogen-Substituted Carbon Materials. *J. Phys. Chem. B* **2005**, *109* (35), 16744−16749.
(42) Preda, I.; Gutiérrez, A.; Abbate, M.; Yubero, F.; Méndez, J.; Alvarez, L.; Soriano, L. Interface Effects in the Ni 2p X-Ray Photoelectron Spectra of NiO Thin Films Grown on Oxide Substrates. *Phys. Rev. B* **2008**, *77* (7), 075411.
(43) Kumar, R.; Sahoo, B. Nano-Structures & Nano-Objects Carbon Nanotubes or Carbon Globules: Optimization of the Pyrolytic Synthesis Parameters and Study of the Magnetic Properties. *Nano-Struct. Nano-Objects* **2018**, *14*, 131−137.
(44) Kichambare, P.; Kumar, J.; Rodrigues, S.; Kumar, B. Electrochemical Performance of Highly Mesoporous Nitrogen Doped Carbon Cathode in Lithium-Oxygen Batteries. *J. Power Sources* **2011**, *196* (6), 3310−3316.
(45) Nxumalo, E. N.; Nyamori, V. O.; Coville, N. J. CVD Synthesis of Nitrogen Doped Carbon Nanotubes Using Ferrocene/Aniline Mixtures. *J. Organomet. Chem.* **2008**, *693* (17), 2942−2948.
(46) Nandan, R.; Gautam, A.; Tripathi, S.; Nanda, K. K. A Comprehensive Analysis and Rational Designing of Efficient Fe-Based Oxygen Electrocatalysts for Metal-Air Batteries. *J. Mater. Chem. A* **2018**, *6* (18), 8537−8548.
(47) Nandan, R.; Nanda, K. K. Designing N-Doped Carbon Nanotubes and Fe-Fe_3C Nanostructures Co-Embedded in B-Doped Mesoporous Carbon as an Enduring Cathode Electrocatalyst for Metal-Air Batteries. *J. Mater. Chem. A* **2017**, *5* (32), 16843−16853.
(48) Zhang, L.; Liu, L. L.; Feng, J. J.; Wang, A. J. Methanol-Induced Assembly and Pyrolysis Preparation of Three-Dimensional N-Doped Interconnected Open Carbon Cages Supported $FeNb_2O_6$ Nanoparticles for Boosting Oxygen Reduction Reaction and Zn-Air Battery. *J. Colloid Interface Sci.* **2024**, *661*, 102−112.
(49) Mahour, L. N.; Choudhary, H. K.; Kumar, R.; Anupama, A. V.; Sahoo, B. Structural, Optical and Mössbauer Spectroscopic Investigations on the Environment of Fe in Fe-Doped ZnO ($Zn_{1-X}Fe_xO$) Ceramics Synthesized by Solution Combustion Method. *Ceram. Int.* **2019**, *45* (18), 24625−24634.
(50) Kumar, A.; Kumar, R.; Verma, N.; Anupama, A. V.; Choudhary, H. K.; Philip, R.; Sahoo, B. Effect of the Band Gap and the Defect States Present within Band Gap on the Non-Linear Optical Absorption Behaviour of Yttrium Aluminium Iron Garnets. *Opt. Mater.* **2020**, *108*, 110163.
(51) Wu, Y. Peidong Yang Direct Observation of Vapor−Liquid−Solid Nanowire Growth. *J. Am. Chem. Soc.* **2001**, *123*, 3165−3166.
(52) Goldie, S. J.; Coleman, K. S. Graphitization by Metal Particles. *ACS Omega* **2023**, *8*, 3278.
(53) Arjmand, M.; Chizari, K.; Krause, B.; Pötschke, P.; Sundararaj, U. Effect of Synthesis Catalyst on Structure of Nitrogen-Doped Carbon Nanotubes and Electrical Conductivity and Electromagnetic Interference Shielding of Their Polymeric Nanocomposites. *Carbon* **2016**, *98*, 358−372.
(54) Kumar, C. N. S.; Chakravadhanula, V. S. K.; Riaz, A.; Dehm, S.; Wang, D.; Mu, X.; Flavel, B.; Krupke, R.; Kübel, C. Understanding the Graphitization and Growth of Free-Standing Nanocrystalline Graphene Using: In Situ Transmission Electron Microscopy. *Nanoscale* **2017**, *9* (35), 12835−12842.
(55) Ai, K.; Li, Z.; Li, W.; Fan, J.; Cui, X.; Zheng, W. Robust Synthesis of High-Performance N-Graphite Hollow Nanocatalysts Based on the Ostwald Ripening Mechanism for Oxygen Reduction Reaction Electrocatalysis. *Part. Part. Syst. Charact.* **2018**, *35* (10), 1800266.
(56) Kumar, R.; Anupama, A. V.; Kumaran, V.; Sahoo, B. Effect of Solvents on the Structure and Magnetic Properties of Pyrolysis Derived Carbon Globules Embedded with Iron/Iron Carbide Nanoparticles and Their Applications in Magnetorheological Fluids. *Nano-Struct. Nano-Objects* **2018**, *16*, 167−173.
(57) Eom, J.-Y.; Jang, J. M.; Paek, M. K.; Pak, J. J. Nitrogen Solubility in Liquid Mn-Fe-Si-C Alloys. *TMS Annu. Meet.* **2014**, *54* (1), 669−674.
(58) Speelmanns, I. M.; Schmidt, M. W.; Liebske, C. Nitrogen Solubility in Core Materials. *Geophys. Res. Lett.* **2018**, *45* (15), 7434−7443.
(59) Kumar, R.; Sahoo, B. One-Step Pyrolytic Synthesis and Growth Mechanism of Core−Shell Type Fe/Fe_3C-Graphite Nanoparticles-Embedded Carbon Globules. *Nano-Struct. Nano-Objects* **2018**, *16*, 77−85.
(60) Das, D.; Santra, S.; Nanda, K. K. In Situ Fabrication of a Nickel/Molybdenum Carbide-Anchored N-Doped Graphene/CNT Hybrid: An Efficient (Pre)Catalyst for OER and HER. *ACS Appl. Mater. Interfaces* **2018**, *10* (41), 35025−35038.
(61) Chen, R.; Yang, C.; Cai, W.; Wang, H. Y.; Miao, J.; Zhang, L.; Chen, S.; Liu, B. Use of Platinum as the Counter Electrode to Study the Activity of Nonprecious Metal Catalysts for the Hydrogen Evolution Reaction. *ACS Energy Lett.* **2017**, *2* (5), 1070−1075.
(62) Yuan, C.-Z.; Jiang, Y.-F.; Wang, Z.; Xie, X.; Yang, Z.-K.; Yousaf, A. B.; Xu, A. W. Cobalt Phosphate Nanoparticles Decorated with Nitrogen-Doped Carbon Layers as Highly Active and Stable Electrocatalysts for the Oxygen Evolution Reaction. *J. Mater. Chem. A* **2016**, *4* (21), 8155−8160.
(63) Bian, J.; Sun, C. NiCoFeP Nanofibers as an Efficient Electrocatalyst for Oxygen Evolution Reaction and Zinc−Air Batteries. *Adv. Energy Sustain. Res.* **2021**, *2* (6), 2000104.
(64) Kumar, S.; Kumar, R.; Goyal, N.; Vazhayil, A.; Yadav, A.; Thomas, N.; Sahoo, B. N-Doped Carbon Nanotubes Nucleated through Cobalt Nanoparticles as Bifunctional Catalysts for Zinc-Air Batteries. *ACS Appl. Nano Mater.* **2024**, *7* (7), 7865−7882.
(65) Ul Haq, M.; Wu, D. H.; Ajmal, Z.; Ruan, Q. D.; Khan, S.; Zhang, L.; Wang, A. J.; Feng, J. J. Derived-2D $Nb_4C_3T_x$ Sheets with Interfacial Self-Assembled Fe-N-C Single-Atom Catalyst for Electrocatalysis in Water Splitting and Durable Zinc-Air Battery. *Appl. Catal. B Environ.* **2024**, *344*, 123632.
(66) Barman, B. K.; Das, D.; Nanda, K. K. Facile and One-Step Synthesis of a Free-Standing 3D MoS_2-RGO/Mo Binder-Free Electrode for Efficient Hydrogen Evolution Reaction. *J. Mater. Chem. A* **2017**, *5* (34), 18081−18087.
(67) Jia, Y.; Gao, X.; Teng, C.; Li, X.; Liu, Y.; Zhi, M.; Hong, Z. Co_2Ni Alloy/N-Doped CNTs Composite as Efficient Hydrogen Evolution Reaction Catalyst in Alkaline Medium. *J. Alloys Compd.* **2019**, *791*, 779−785.
(68) Guo, Y.; Zhang, X.; Zhang, X.; You, T. Defect- and S-Rich Ultrathin MoS_2 Nanosheet Embedded N-Doped Carbon Nanofibers for Efficient Hydrogen Evolution. *J. Mater. Chem. A* **2015**, *3* (31), 15927−15934.
(69) Chen, W.; Qiao, R.; Song, C.; Zhao, L.; Jiang, Z. J.; Maiyalagan, T.; Jiang, Z. Tailoring the Thickness of $MoSe_2$ Layer of the Hierarchical Double-Shelled N-Doped Carbon@$MoSe_2$ Hollow Nanoboxes for Efficient and Stable Hydrogen Evolution Reaction. *J. Catal.* **2020**, *381*, 363−373.
(70) Gao, M.-R.; Chan, M. K. Y.; Sun, Y. Edge-Terminated Molybdenum Disulfide with a 9.4-Å Interlayer Spacing for Electrochemical Hydrogen Production. *Nat. Commun.* **2015**, *6* (1), 7493.
(71) Chen, H.; Liang, X.; Liu, Y.; Ai, X.; Asefa, T.; Zou, X. Active Site Engineering in Porous Electrocatalysts. *Adv. Mater.* **2020**, *32* (44), 2002435.
(72) Jia, Y.; Jiang, K.; Wang, H.; Yao, X. The Role of Defect Sites in Nanomaterials for Electrocatalytic Energy Conversion. *Chem* **2019**, *5* (6), 1371−1397.
(73) Zhu, J.; Mu, S. Defect Engineering in Carbon-Based Electrocatalysts: Insight into Intrinsic Carbon Defects. *Adv. Funct. Mater.* **2020**, *30* (25), 2001097.
(74) Santra, S.; Das, D.; Das, N. S.; Nanda, K. K. An Efficient On-Board Metal-Free Nanocatalyst for Controlled Room Temperature Hydrogen Production. *Chem. Sci.* **2017**, *8* (4), 2994−3001.
(75) Cheng, X.; Shen, Z.; Jiao, L.; Yang, L.; Wang, X.; Wu, Q.; Hu, Z. Tuning Metal Catalysts via Nitrogen-Doped Nanocarbons for Energy Chemistry: From Metal Nanoparticles to Single Metal Sites. *EnergyChem* **2021**, *3* (6), 100066.

https://doi.org/10.1021/acsanm.4c02278
ACS Appl. Nano Mater. XXXX, XXX, XXX−XXX

(76) Koster, D.; Zeradjanin, A. R.; Battistel, A.; La Mantia, F. Extracting the Kinetic Parameters of the Hydrogen Evolution Reaction at Pt in Acidic Media by Means of Dynamic Multi-Frequency Analysis. *Electrochim. Acta* **2019**, *308*, 328−336.
(77) Panek, J.; Serek, A.; Budniok, A.; Rówinski, E.; Łagiewka, E. Ni + Ti Composite Layers as Cathode Materials for Electrolytic Hydrogen Evolution. *Int. J. Hydrogen Energy* **2003**, *28* (2), 169−175.
(78) Jukic, A.; Metikoš-Hukovic, M. The Hydrogen Evolution Reaction on Pure and Polypyrrole-Coated $GdNi_4Al$ Electrodes. *Electrochim. Acta* **2003**, *48* (25−26), 3929−3937.
(79) *Faulkner, L. R.*; Allen, J. B. *Electrochemical Methods Fundamentals and Applications*, 2nd nd ed., Swain, E.; John Wiley & Sons, Inc: Texas, Austin, 1980.
(80) Henrique, F.; Zuk, P. J.; Gupta, A. Charging Dynamics of Electrical Double Layers inside a Cylindrical Pore: Predicting the Effects of Arbitrary Pore Size. *Soft Matter* **2021**, *18* (1), 198−213.
(81) Birry, L.; Lasia, A. Studies of the Hydrogen Evolution Reaction on Raney Nickel-Molybdenum Electrodes. *J. Appl. Electrochem.* **2004**, *34* (7), 735−749.
(82) Song, H. K.; Jung, Y. H.; Lee, K. H.; Dao, L. H. Electrochemical Impedance Spectroscopy of Porous Electrodes: The Effect of Pore Size Distribution. *Electrochim. Acta* **1999**, *44* (20), 3513−3519.

https://doi.org/10.1021/acsanm.4c02278
ACS Appl. Nano Mater. XXXX, XXX, XXX−XXX